EPR Study of the Molecular and Electronic Structure of the Semiquinone Biradical $Q_A^{-\bullet}Q_B^{-\bullet}$ in Photosynthetic Reaction Centers from *Rhodobacter sphaeroides*

Rafael Calvo,[†,‡] Edward C. Abresch,[†] Robert Bittl,[§] George Feher,[*,†] Wulf Hofbauer,[§] Roger A. Isaacson,[†] Wolfgang Lubitz,[§] Melvin Y. Okamura,[†] and Mark L. Paddock[†]

Contribution from the Department of Physics, University of California, San Diego, 9500 Gilman Drive, La Jolla, California 92093-0319, Departamento de Física, Facultad de Bioquímica y Ciencias Biológicas, Universidad Nacional del Litoral, and INTEC (CONICET-UNL), Güemes 3450, 3000 Santa Fe, Argentina, and Max-Volmer-Institut für Biophysikalische Chemie und Biochemie, Technische Universität Berlin, D-10623 Berlin, Germany

Received February 2, 2000. Revised Manuscript Received May 30, 2000

Abstract: The photocycle of bacterial photosynthetic reaction centers (RCs) involves electron transfer between two quinone molecules, Q_A and Q_B. The semiquinone biradical $Q_A^{-\bullet}Q_B^{-\bullet}$ forms an intermediate state in this process. We trapped the biradical at low temperature (77 K) and investigated its EPR spectra at three microwave frequencies, 9.6, 35, and 94 GHz, at temperatures between 1.5 and 100 K. The spectra were described with a spin Hamiltonian that contained, in addition to the Zeeman terms, dipolar and exchange interactions, and were fitted using the simulated annealing method (Kirkpatrick et al. *Science* **1983**, *220*, 671). From the parameters derived from the fit, information about the spatial and electronic structure was obtained. The relative position and orientation of the two quinones, determined from the EPR spectra, compared well with those obtained from X-ray diffraction of RCs in the $Q_AQ_B^{-\bullet}$ state (Stowell et al. *Science* **1997**, *276*, 812). The values of the dipolar coupling and of the exchange interaction obtained from the fits were $E_d/h = (10.3 \pm 0.1)$ MHz and $J_o/h = (-60 \pm 20)$ MHz, respectively. The value of J_o was used to estimate a maximum electron-transfer rate, k_{ET}, ($Q_A^{-\bullet}Q_B^{-\bullet} \rightarrow Q_AQ_B^{=}$) of $\sim 10^9$ s^{-1}. This agrees within an order of magnitude with the value derived from kinetics experiments (Graige et al. *Biochemistry* **1999**, *38*, 11465).

Introduction

The photosynthetic reaction center (RC) from bacteria is a membrane-bound pigment protein complex that performs the primary photochemistry by coupling light-induced electron transfer to vectorial proton transfer across the bacterial membrane. In the RC from the bacterium *Rhodobacter sphaeroides* (see Figure 1), light-induced electron-transfer proceeds from a primary donor (a bacteriochlorophyll dimer, D),[1] through a series of electron acceptor molecules (a bacteriopheophytin ϕ and a quinone molecule Q_A), to a loosely bound secondary quinone (Q_B) which serves as a mobile electron and proton carrier.[2,3]

The RC catalyzes a two-electron/two-proton reduction of the secondary quinone Q_B, following the absorption of two photons:

$$Q_B + 2e^- + 2H^+ + 2h\nu \rightarrow Q_BH_2 \qquad (1)$$

The process described by eq 1 involves several intermediate states, including the biradical state $Q_A^{-\bullet}Q_B^{-\bullet}$.[4] To understand the mechanism of electron transfer between the semiquinones, a knowledge of the *spatial* as well as the *electronic* structure of the biradical is important. The spatial structure of the ground-state DQ_AQ_B has been determined by X-ray diffraction by several authors.[5−12] However, only two intermediate states have so far been trapped and studied in single crystals by X-ray

* To whom correspondence should be addressed. Telephone: (858) 534-4388. Fax: (858) 822-0007. E-mail: gfeher@physics.ucsd.edu.
† University of California, San Diego.
‡ Universidad Nacional del Litoral and CONICET.
§ Technische Universität Berlin.

(1) Abbreviations: D = $BChl_2$ = bacteriochlorophyll primary donor; ϕ_A = $BPhe_A$ = bacteriopheophytin intermediate acceptor; Q_A and Q_B = primary and secondary quinone acceptors (coenzyme Q-10); $Q_A^{-\bullet}$ and $Q_B^{-\bullet}$ = Q_A and Q_B semiquinone radicals; J_o = exchange interaction parameter; $E_d = g^2\mu_B 2/R^3$, magnitude of the dipolar interaction; ϕ_E, θ_E, ψ_E = Euler angles relating $Q_A^{-\bullet}$ to $Q_B^{-\bullet}$; **R** = vector connecting the centers of the two semiquinone planes; θ_R and ϕ_R = orientation of the vector **R** relating the origin of the $Q_B^{-\bullet}$ axis system to that of $Q_A^{-\bullet}$; ΔB = peak to peak line width of $d\chi''/dB$.; φ_A and φ_B = magnetic orbitals centered in $Q_A^{-\bullet}$ and $Q_B^{-\bullet}$ which describe the EPR spectra of the quinones.

(2) Feher, G.; Allen, J. P.; Okamura, M. Y.; Rees, D. C. *Nature* **1989**, *339*, 111−116.
(3) Blankenship, R. E.; Madigan, M. T.; Bauer, C. E. *Anoxygenic Photosynthetic Bacteria*; Blankenship, R. E., Madigan, M. T., Bauer, C. E., Eds.; Kluwer Academic: Dordrecht, The Netherlands, 1995; Part 5.
(4) Okamura, M. Y.; Feher, G. *Annu. Rev. Biochem.* **1992**, *61*, 861−896.
(5) Allen, J. P.; Feher, G.; Yeates, T. O.; Rees, D. C.; Deisenhofer, J.; Michel, H.; Huber, R. *Proc. Natl. Acad. Sci. U.S.A.* **1986**, *83*, 8589−8593.
(6) Chang, C. H.; Tiede, D.; Tang, J.; Smith, U.; Norris, J. R.; Schiffer, M. *FEBS Lett.* **1986**, *205*, 82−86.
(7) Allen, J. P.; Feher, G.; Yeates, T. O.; Komiya, H.; Rees, D. C. *Proc. Natl. Acad. Sci. U.S.A.* **1987**, *84*, 5730−5734.
(8) Allen, J. P.; Feher, G.; Yeates, T. O.; Komiya, H.; Rees, D. C. *Proc. Natl. Acad. Sci. U.S.A.* **1987**, *84*, 6162−6166.
(9) Yeates, T. O.; Komiya, H.; Rees, D. C.; Allen, J. P.; Feher, G. *Proc. Natl. Acad. Sci. U.S.A.* **1987**, *84*, 6438−6442.
(10) Allen, J. P.; Feher, G.; Yeates, T. O.; Komiya, H.; Rees, D. C. *Proc. Natl. Acad. Sci. U.S.A.* **1988**, *85*, 8487−8491.
(11) Yeates, T. O.; Komiya, H.; Chirino, A.; Rees, D. C.; Allen, J. P.; Feher, G. *Proc. Natl. Acad. Sci. U.S.A.* **1988**, *85*, 7993−7997.
(12) Ermler, U.; Fritzsch, G.; Buchanan, S. K.; Michel, H. *Structure* **1994**, *2*, 925−936.

10.1021/ja000399r CCC: $19.00
Published on Web 07/13/2000

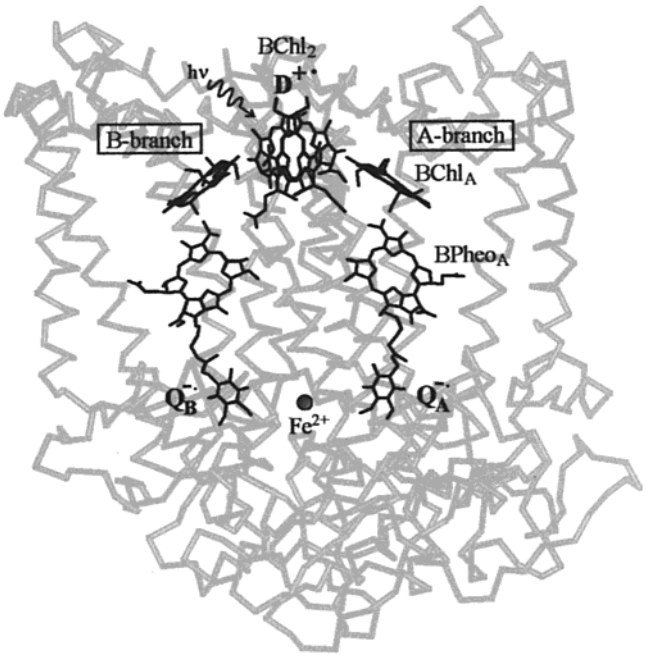

Figure 1. Structure of the cofactors in the photosynthetic reaction center of *Rb. sphaeroides*, with the protein polypeptide chains in the background.[13] Electron-transfer proceeds along the A-branch from $(BChl)_2$ (D) through $BChl_A$, $BPheo_A$ (ϕ_A), Q_A, to Q_B. In the work reported here Fe^{2+} was replaced by Zn^{2+}.

diffraction. These are $D^+Q_AQ_B^{-\bullet}$,[13] and $D^+Q_A^{-\bullet}$.[14] The biradical state $Q_A^{-\bullet}Q_B^{-\bullet}$ is difficult to produce and trap in single crystals. We were, however, able to trap it in frozen solution of randomly oriented RCs. From the EPR spectra of this biradical, information on both, the spatial and the electronic structure were obtained, as discussed below.

The EPR spectrum of a biradical is to a large extent determined by the interaction between the two spins, which can be divided into two types. One is the dipolar interaction, which is directly related to the geometry, that is, distance and angles, of the two interacting spins.[15] Consequently, a determination of the dipolar interaction provides structural information of the biradical. The second type is the exchange interaction, which is related to matrix elements between the magnetic orbitals, which provide the exchange path through which the two spins interact.[16−19] Thus, the magnitude of the exchange interaction gives information about the electronic structure of the biradical, in particular about the path connecting the two spins, which is important for understanding the electron transfer between the quinones. This type of information is difficult to obtain from any other experimental measurement.

Magnetic interactions between photocycle intermediates have been studied by a number of groups to obtain structural and electronic information.[20−32] For example, prior to the determination of the crystal structure of the RC (Figure 1), Butler et al predicted the symmetric arrangement of $Q_A^{-\bullet}$ and $Q_B^{-\bullet}$ with respect to the Fe^{2+} ion, based on similar interactions between Fe^{2+} and each of the quinone acceptors.[23,24,32] Magnetic and structural information was obtained from time-resolved EPR experiments[33] by Dzuba et al.,[25,29,30] Zech et al.,[27] and Bittl and Zech[28] to estimate distances between the primary donor and acceptor in RC of *Rb. sphaeroides* and photosystem I of *Synechococcus elongatus*. The electronic information, obtained from a magnetic study was related to function by Okamura et al.[34] These authors presented and successfully tested a simple model which relates the magnitude J_o of the exchange interaction between $Q_A^{-\bullet}$ and $BPheo_A^{-\bullet}$ to the electron-transfer rate between $BPheo_A^{-\bullet}$ and $Q_A^{-\bullet}$.

In this work, we generated a different intermediate, the $Q_A^{-\bullet}Q_B^{-\bullet}$ biradical in frozen solution of RCs from *Rb sphaeroides* R26 in which the paramagnetic Fe^{2+} was replaced by diamagnetic Zn^{2+}. This reduces the line width by more than 2 orders of magnitude. The biradical was produced by chemical and by light reduction, and its EPR spectra were obtained at different microwave frequencies (9.6, 35, and 94 GHz), and different temperatures (100 K $\geq T \geq$ 1.5 K). We modeled the system with a spin Hamiltonian from which the expected EPR spectra were calculated. By fitting the calculated spectra with the experimental spectra, values for the dipolar and the exchange interactions were obtained. The spatial structure of $Q_A^{-\bullet}Q_B^{-\bullet}$, derived from the parameters of the dipolar interaction, was compared with the X-ray structure of $Q_AQ_B^{-\bullet}$ obtained by Stowell et al.,[13] shown in Figure 1. The value of J_o was used to estimate a maximum electron-transfer rate between the semiquinones, which was compared with estimates obtained from other, independent experiments.[35,36] Preliminary accounts of this work have been presented.[37,38]

(13) Stowell, M. H. B.; McPhillips, T. M.; Rees, D. C.; Soltis, S. M.; Abresch, E.; Feher, G. *Science* **1997**, *276*, 812−816.
(14) Abresch, E. C.; Yeh, A. P.; Soltis, S. M.; Rees, D. C.; Axelrod, H. L.; Okamura, M. Y.; Feher, G. *Biophys. J.* **1999**, *76*, A141.
(15) Pake, G. E. *Paramagnetic Resonance. An introductory Monograph*; Benjamin: New York, 1962; Chapter 4.
(16) Anderson, P. W. *Phys. Rev.* **1959**, *115*, 2−13.
(17) Zeiger, H. J.; Pratt, G. W. *Magnetic Interactions in Solids*; Clarendon Press: Oxford, 1973.
(18) Hay, P. J.; Thibeault, J. C.; Hoffman, R. *J. Am. Chem. Soc.* **1975**, *97*, 4884−4899.
(19) Kahn, O. *Molecular Magnetism*; Wiley-VCH: New York, 1993; Chapter 8.
(20) Tiede, D. M.; Prince, R. C.; Dutton, P. L. *Biochim. Biophys. Acta* **1976**, *449*, 447−467.
(21) Prince, R. C.; Tiede, D. M.; Thornber, J. P.; Dutton, P. L. *Biochim. Biophys. Acta* **1977**, *462*, 467−490.
(22) Okamura, M. Y.; Isaacson, R. A.; Feher, G. *Biochim. Biophys. Acta* **1979**, *546*, 394−417.
(23) Butler, W. F.; Johnston, D. C.; Shore, H. B.; Fredkin, D. R.; Okamura, M. Y.; Feher, G. *Biophys. J.* **1980**, *32*, 967−992.
(24) Butler, W. F.; Calvo, R.; Fredkin, D. R.; Isaacson, R. A.; Okamura, M. Y.; Feher, G. *Biophys. J.* **1984**, *45*, 947−973.
(25) Dzuba, S. A.; Gast, P.; Hoff, A. J. *Chem. Phys. Lett.* **1995**, *236*, 595−602.
(26) Van den Brink, J. S.; Gast, P.; Hoff, A. J. *J. Chem. Phys.* **1996**, *104*, 1805−1812.
(27) Zech, S. G.; Lubitz, W.; Bittl, R. *Ber. Bunsen-Ges. Phys. Chem.* **1996**, *100*, 2041−2044.
(28) Bittl, R.; Zech, S. G. *J. Phys. Chem. B* **1997**, *101*, 1429−1436.
(29) Dzuba, S. A.; Gast, P.; Hoff, A. J. *Chem. Phys. Lett.* **1997**, *268*, 273−279.
(30) Dzuba, S. A.; Hara, H.; Kawamori, A.; Iwaki, M.; Itoh, S.; Tsvetkov, Y. D. *Chem. Phys. Lett.* **1997**, *264*, 238−244.
(31) Calvo, R.; Isaacson, R. A.; Abresch, E. C.; Okamura, M. Y.; Feher, G. *Biophys. J.* **1999**, *76*, A357.
(32) Feher, G.; Okamura, M. Y. *Appl. Magn. Reson.* **1999**, *16*, 63−100.
(33) Salikhov, K. M.; Bock, C. H.; Stehlik, D. *Appl. Magn. Reson.* **1990**, *1*, 195−211.
(34) Okamura, M. Y.; Fredkin, D. R.; Isaacson, R. A.; Feher, G. in *Tunneling in Biological Systems*; Chance, B., DeVault, D. C., Frauenfelder, H., Marcus, R. A., Schriefer, J. R., Sutin, N., Eds.; Academic Press: New York, 1979; pp 729−743.
(35) Graige, M. S.; Paddock, M. L.; Feher, G.; Okamura, M. Y. *Biochemistry* **1999**, *38*, 11465−11473.
(36) Page, C. C.; Moser, C. C.; Chen, X.; Dutton, P. L. *Nature* **1999**, *402*, 47−52.
(37) Calvo, R.; Paddock, M. L.; Abresch, E.; Isaacson, R. A.; Okamura, M. Y.; Feher, G. *Biophys. J.* **1998**, *74*, A135.
(38) Calvo, R.; Hofbauer, W.; Lendzian, F.; Lubitz, W.; Paddock, M. L.; Abresch, E. C.; Isaacson, R. A.; Okamura, M. Y.; Feher, G. *Biophys. J.* **1999**, *76*, A392.

Materials and Methods

Preparation of Reaction Centers and Production of the Radical States. Reaction centers (RCs) were isolated and the non-heme iron was replaced with diamagnetic Zn^{2+} following the procedure of Debus et al.[39] as modified by Utschig et al.[40] The replacement of paramagnetic Fe^{2+} with diamagnetic Zn^{2+} reduces the EPR line width of the semiquinones. A further reduction of the EPR line width was obtained by replacing the protonated ubiquinone with deuterated ubiquinone (dUQ_{10}:pUQ_{10} = 10:1) and by incubating the RCs for 24 h in D_2O prior to freezing, to allow the replacement of the exchangeable protons with deuterium.

From these RCs, samples containing the $Q_A^{-\bullet}$ and $Q_B^{-\bullet}$ radical states and the $Q_A^{-\bullet}Q_B^{-\bullet}$ biradical state were made. Each sample containing ~3 μL of RC material (A_{805}^{1cm} = 150) was loaded into a Suprasil capillary (0.87 mm o.d., 0.7 mm i.d.; Wilmad no. CV7087S) to fit the 94 GHz spectrometer. To protect the delicate capillaries, they were inserted into standard Q-band tubes (3 mm o.d., 2 mm i.d., Wilmad no. 705PQ) for handling, storage and running at 9.6 and 35 GHz. The $Q_A^{-\bullet}$ and $Q_B^{-\bullet}$ semiquinone samples were made by exciting the RCs with a single saturating laser flash (Lumen X DL2100C, λ = 590 nm, ~0.2 J/pulse, 0.4 μs full-width at half-maximum) in the presence of excess cyt c to reduce the donor, D^+, prior to freezing, leaving only the semiquinone radical in the RC. The $Q_A^{-\bullet}$ and $Q_B^{-\bullet}$ semiquinone samples were made with or without stigmatellin (a Q_B site inhibitor), respectively. Biradical samples $Q_A^{-\bullet}Q_B^{-\bullet}$ were made by two methods. One method involved the light induced formation of the biradical state. RCs in the presence of cyt c^{2+} were given a single laser flash to generate the cyt $c^{2+}DQ_AQ_B^{-\bullet}$ state in those RCs with a bound Q_B molecule (~80% of the RC sample); the oxidized cyt c^{3+} generated during the photochemistry exchanges with exogenous cyt c^{2+} in the solution prior to freezing the sample at 77 K. Illumination of this sample in the frozen state at 190 K generated the cyt $c^{3+}DQ_A^{-\bullet}Q_B^{-\bullet}$ state; electron transfer between the quinones does not occur to any appreciable extent at these low temperatures. The second method involved chemical reduction of the quinones. The addition of $NaBH_4$ reduces Q_B to form $Q_B^{=}$ without reacting with Q_A. An equilibrium is established between the EPR silent state $Q_AQ_B^{=}$ and the EPR active state $Q_A^{-\bullet}Q_B^{-\bullet}$.[41,42] This equilibrium is pH dependent and favors the formation of the $Q_A^{-\bullet}Q_B^{-\bullet}$ state above pH8.5. Following chemical reduction by $NaBH_4$ for ~2 min, the samples were frozen and stored in liquid nitrogen. A series of EPR samples were made from pH 7.5−10.5 to monitor the EPR amplitude of the biradical state as a function of pH. The pH was adjusted by adding 100 mM Hepes pH 7.5 (*N*-[2-hydroxyethyl] piperazine-*N*′-[2-ethane sulfonic acid]), 100 mM Tris pH 8.5 (2-amino-2-(hydroxymethyl) propane-1,3-diol), 100 mM Ches pH 9.5 (cyclohexylaminoethane sulfonic acid), or 100 mM Caps pH 10.5 (3-cyclohexylamino-1-propanesulfonic acid). The $Q_A^{-\bullet}Q_B^{-\bullet}$ biradical spectra shown in the Results section were obtained at pH10.5. Using the methods described above, we also prepared samples from RCs of the site-directed mutant having a His(M266) → Cys mutation.[43]

EPR Measurements. Spectra of the RC samples containing either $Q_A^{-\bullet}$, $Q_B^{-\bullet}$ or $Q_A^{-\bullet}Q_B^{-\bullet}$ were obtained at three microwave frequencies, 9.6 GHz (X-band), 35 GHz (Q-band) and 94 GHz (W-band). The same sample of each species was run at all three frequencies. Experiments at X and Q-band were performed in San Diego and at W-band in Berlin.

The 9.6 GHz spectrometer is of local design with superheterodyne detection,[44] with the addition of a low noise microwave preamplifier (Mitek, AMF-3B-8012-25) and a YIG oscillator (Avantek, S080-1258) instead of a klystron for the microwave source. The cavity was replaced by a dielectric ring resonator[45−47] to improve the filling factor associated with the small samples, whose size was dictated by the 94 GHz cavity. The dielectric ring is composed of two stacked rings, similar to those described previously.[48] The standard 2 mm hole was enlarged to 3 mm with an ultrasonic impact grinder. The 3 mm diameter hole permitted the use of standard Q-band sample tubes into which the 0.7 mm capillary, containing the sample, was inserted. The 9.6 GHz resonator is coupled directly to the waveguide via a Gordon coupler.[49,50] For temperature control, a double glass dewar cryostat was used, with liquid nitrogen in the outer dewar. At 80 K, the inner dewar is backfilled with gaseous nitrogen. To compare data taken at the different microwave frequencies, the absolute values of the magnetic field had to be determined with high accuracy. This was accomplished by using, as the primary standard for all *g*-value measurements, a Li:LiF sample with g = 2.00229(1).[51] High precision *g*-value data were obtained with a LabView program run on a PC, that controlled the field and performed the signal averaging. This system resets the scan center field between each 30 s scan by processing the output from an NMR teslameter, and microwave frequency counter (EIP 548A). The field sweep limits were also measured from scan to scan with the teslameter, which was connected via GPIB to the PC.

At 35 GHz, we used a TE_{011} brass cavity and coupler, similar to one described before.[52] In addition to the Li:LiF, P-doped Si was used as a secondary *g*-value standard (g = 1.99891 at 80 K, and 1.99865 at or below 4.2 K).[53,54] The P−Si marker was permanently attached to the bottom wall of the 35 GHz TE_{011} cavity. The cryostat and data collection systems are identical to those used at 9.6 GHz. The resonator and sample were submerged in liquid He. Temperatures below 4.2 K were obtained by pumping on the inner dewar through a precision needle valve; temperatures were determined from the He vapor pressure. At these low temperatures, very low microwave powers (0.2−1 nW) had to be used to avoid saturation. At these powers, the normal automatic frequency control (AFC) circuit is not effective and manual tuning was required to obtain a pure EPR absorption signal.

The 94 GHz EPR measurements were performed using a commercial Bruker E680 spectrometer, which is capable of working in either CW or pulsed mode. The instrument uses superheterodyne detection with an intermediate frequency (IF) of 9.5 GHz. The resonance microwave frequency was determined by measuring the IF frequency with a frequency counter and adding it to the frequency of the local oscillator (84.500814 GHz), which is locked to a precision quartz reference. No AFC was used since the frequency drift of the free-running microwave source is only a few kHz during data acquisition. The height of the cylindrical TE_{011} cavity is adjustable to compensate for the frequency shift caused by insertion of the sample. Critical coupling is achieved by a movable short in the waveguide. The Suprasil sample tubes are introduced into the resonator along the cylindrical axis for about 3 mm, resulting in an effective sample volume of ~0.5 μL. The cavity assembly is contained in an Oxford helium cryostat. A split coil, wide-bore hybrid magnet system is used. It has resistive auxiliary coils for a maximum 80 mT sweep, while leaving the superconducting coils in a persistent mode (at 3.36 T for g = 2). Field calibrations were obtained by measuring a Li:LiF *g*-marker at two microwave frequencies about 0.3 GHz apart and using linear interpolation for the current/field relationship. Secondary field calibrations were made using powdered Mn^{2+}:MgO, which exhibits six hyperfine lines with accurately known

(39) Debus, R. J.; Feher, G.; Okamura, M. Y. *Biochemistry* **1986**, *25*, 2276−2287.
(40) Utschig, L. M.; Greenfield, S. R.; Tang, J.; Laible, P. D.; Thurnauer, M. C. *Biochemistry* **1997**, *36*, 8548−8558.
(41) Kleinfeld, D.; Okamura, M. Y.; Feher, G. *Biochem. Biophys. Acta* **1985**, *809*, 291−310.
(42) McPherson, P. H.; Schönfeld, M.; Paddock, M. L.; Okamura, M. Y.; Feher, G. *Biochemistry* **1994**, *33*, 1181−1193.
(43) Williams, J. C.; Paddock, M. L.; Feher, G.; Allen, J. P. *Biophys. J.* **1991**, *59*, 142a.
(44) Feher, G. *Bell Syst. Tech. J.* **1957**, *36*, 449−484.
(45) Dykstra, R. W.; Markham, G. D. *J. Magn. Reson.* **1986**, *69*, 350−355.
(46) Walsh, W. M., Jr.; Rupp, L. W., Jr. *Rev. Sci. Instrum.* **1986**, *57*, 2278−2279.
(47) Sienkiewicz, A.; Qu, K. B.; Scholes, C. P. *Rev. Sci. Instrum.* **1994**, *65*, 68−74.
(48) Jaworski, M.; Sienkiewicz, A.; Scholes, C. P. *J. Magn. Reson.* **1997**, *124*, 87−96.
(49) Gordon, J. P. *Rev. Sci. Instrum.* **1961**, *32*, 658−661.
(50) Isaacson, R. A. *Rev. Sci. Instrum.* **1976**, *47*, 973−974.
(51) Stesmans, A.; Van Gorp, G. *Rev. Sci. Instrum.* **1989**, *60*, 2949−2952.
(52) Sienkiewicz, A.; Smith, B. G.; Veselov, A.; Scholes, C. P. *Rev. Sci. Instrum* **1996**, *67*, 2134−2138.
(53) Feher, G.; Gere, E. A. *Phys. Rev.* **1959**, *114*, 1245−1256.
(54) Stesmans, A.; De Vos, G. *Phys. Rev. B* **1986**, *34*, 6499−6502.

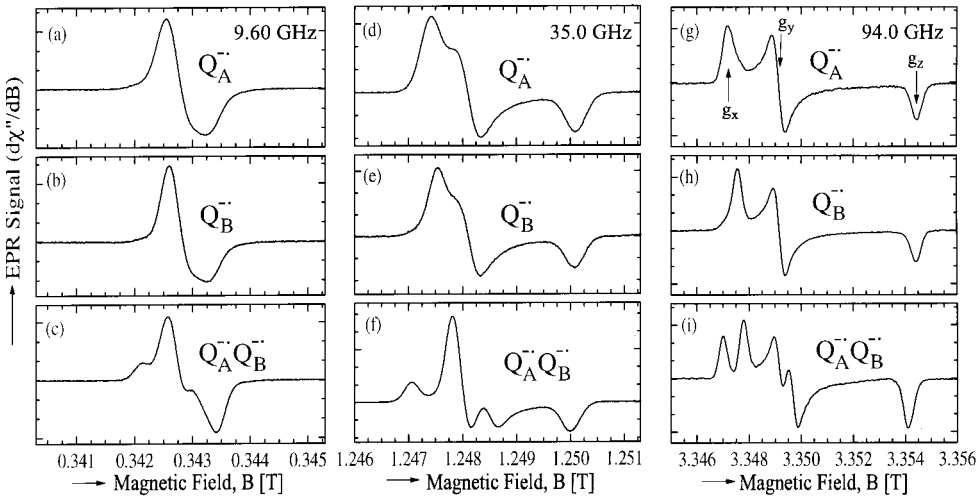

Figure 2. EPR spectra of $Q_A^{-\bullet}$ (a, d, g), $Q_B^{-\bullet}$ (b, e, h) and $Q_A^{-\bullet}Q_B^{-\bullet}$ (c, f, i), at 9.6, 35 and 94 GHz, in RCs of *Rb. sphaeroides*, at $T = 80$ K. In (g) the peaks corresponding to the principal directions of the *g*-tensor of $Q_A^{-\bullet}$ are labeled. Note the increase of resolution with increasing frequency. The spectra of $Q_A^{-\bullet}Q_B^{-\bullet}$ are not a superposition of the individual $Q_A^{-\bullet}$ and $Q_B^{-\bullet}$ spectra, reflecting the magnetic interaction between $Q_A^{-\bullet}$ and $Q_B^{-\bullet}$.

splittings.[55] Using this procedure, the field reproducibility was ≤0.03 mT. At low temperatures (≤20 K), it was difficult to obtain CW spectra without significant distortions due to saturation effects. Consequently, field-swept two-pulse ($2\pi/3 - \tau - 2\pi/3$, $\tau = 400$ ns) ESE (electron spin−echo) experiments were performed. By using low repetition rates (5 s^{-1}) at 5 K, the spin system was given sufficient time to return to thermal equilibrium before applying the next pulse. Due to the large spin polarization ($k_BT \approx h\nu$ at $T = 5$ K and $\nu = 94$ GHz), few accumulations (64) were required to obtain a satisfactory signal/noise ratio.

Numerical Fitting Procedures. The Simulated Annealing Method. To compare experimental with calculated (simulated) EPR spectra we divide the spectrum into *N* intervals, that is, we treat the spectrum as a *N*-dimensional vector **A** where each component A_j has the amplitude of the EPR signal at a magnetic field $B_j = B_{min} + (j - 1)\Delta$, with *j* varying from 1 to *N*. The field interval is defined as $\Delta = (B_{max} - B_{min})/(N - 1)$, where B_{max} and B_{min} are the maximum and minimum magnetic fields of the spectrum. In all cases $N \approx 1000$. We normalized the amplitudes of the spectra (experimental and simulated) so that the span between the maximum and minimum values of A_j is one. When simulating a spectrum we compared the calculated amplitude A_j^{calc} of the signal with the observed value at each interval B_j. We define a root-mean-square deviation or quality factor of a simulation by

$$\sigma(p_1, p_2, ..., p_n) = [\sum_j (A_j^{calc}(p_1, p_2, .., p_n) - A_j^{exp})^2/N]^{1/2} \qquad (2)$$

where the sums are over the *N* field values *j*, and p_α are the parameters that produced the calculated spectrum. Due to the expected complexity and nonlinearity of the problem, one may find local minima of σ for different parameter sets p_α. Thus, the use of standard methods, which allow a change in the value of the parameter p_α only when the calculated σ is reduced, may not result in an absolute minimum. One can be trapped in a local minimum, which is unrelated to the global minimum. Indeed, we found many local minima. To circumvent similar problems, Kirkpatrick et al.[56] proposed the "simulated annealing" method[57] based on the Metropolis algorithm.[58] Detailed descriptions of the method are given by Press et al.[59] Application of the method to spectral simulation has been reported by Hustedt et al.[60] The error function σ defined by eq 2 (the "cost" function in the analysis of Kirkpatrick et al.[56]), is calculated as a function of the parameters which are varied one by one in a given sequence. This variation is made randomly within a "reasonable" range defined a priori. Each time that a proposed set of parameters produces a smaller value of σ, it is chosen as the "best set". When the new value of $\sigma(p_\alpha)$ is larger than that of the best set, it is not automatically discarded as is done in standard methods. Instead, the new parameter set is assigned a probability *P* of being accepted. Defining $\Delta\sigma$ as the difference between the new $\sigma(p_\alpha)$ and the value of σ obtained for the already accepted best set of parameters, a Boltzmann-like probability is defined as $P \approx \exp(-\Delta\sigma/k_BT_\sigma)$ ($0 \le P \le 1$ for $\Delta\sigma > 0$, k_B is the Boltzmann constant). This allows σ to increase and to get out of a local minimum. The parameter T_σ, which simulates the temperature in the annealing process, is reduced slowly while the value of $\sigma(p_\alpha)$ is calculated for many sets of p_α (see Analysis section).

A FORTRAN routine was written that calculates the values A_j^{calc} of the spectrum for each input set of values p_α, at a given T_σ. An "annealing" main program changes the values of the input parameters in a random fashion within a given interval, searching for a value of $\sigma(p_\alpha)$ close to the absolute minimum, while slowly decreasing T_σ. To perform a fit, the quality factor $\sigma(p_\alpha)$ of eq 2 was minimized either for a single spectrum, or for several spectra taken at different microwave frequencies and different temperatures (global fit).

EPR Results

EPR spectra of $Q_A^{-\bullet}$, $Q_B^{-\bullet}$ and $Q_A^{-\bullet}Q_B^{-\bullet}$ were obtained at three microwave frequencies in randomly oriented frozen samples of reaction centers of *Rb. sphaeroides* R26. Figure 2 displays the EPR signals ($d\chi''$/dB) vs magnetic field *B* at microwave frequencies of 9.6, 35, and 94 GHz, at 80 K.[61] In Figure 3 the EPR spectra are shown at three temperatures, at 35 and 94 GHz. It was observed that the saturation parameters varied across the spectrum, causing severe distortions of the line shape at low temperature and high powers. Special care

(55) Burghaus, O.; Plato, M.; Bumann, D.; Neumann, B.; Lubitz, W.; Möbius, K. *Chem. Phys. Lett.* **1991**, *185*, 381−386.

(56) Kirkpatrick, S.; Gelatt, C. D.; Vecchi, M. P. *Science* **1983**, *220*, 671−680.

(57) The simulated annealing method can be understood by an analogy with the way in which liquids freeze and crystallize or in which metals cool and anneal. In a liquid at high temperatures the molecules move freely with respect to one another. When the liquid is cooled, the mobility is lost. With slow cooling the atoms have ample time to rearrange themselves, and the system approaches the ground-state energy. A fast cooling may lead to a metastable state having a higher energy (local minimum).

(58) Metropolis, N. A.; Rosenbluth, A.; Rosenbluth, M.; Teller, A.; Teller, E. *J. Chem. Phys.* **1953**, *21*, 1087−1092.

(59) Press, W. H.; Teukolsky, S. A.; Vetterling, W. T.; Flannery, B. P. *Numerical Recipes in FORTRAN: The Art of Scientific Computing*; Cambridge University Press: New York, 1992; Sect. 10.9.

(60) Hustedt, E. J.; Smirnov, A. I.; Laub, C. F.; Cobb, C. E.; Beth, A. H. *Biophys. J.* **1997**, *72*, 1861−1877.

(61) All EPR spectra have been normalized to the same peak-to-peak amplitude.

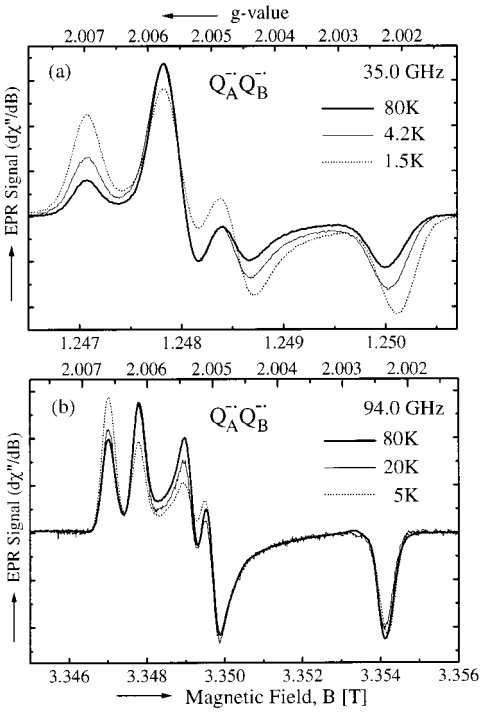

Figure 3. EPR spectra of the $Q_A^{-\bullet}Q_B^{-\bullet}$ biradical, (a) For 35 GHz at various temperatures. Experimental conditions: microwave power = 0.5 μW, field modulation = 0.2 mT at 10 kHz. Traces represent an average of 10 scans, each with an acquisition time of 80 ms/point (typically 1024 points). (b) For 94 GHz at various temperatures. Experimental conditions: At 80 K, CW microwave power = 16 nW, field modulation = 0.2 mT at 10 kHz; 33 ms/point and 32 scans). At 20 K and below, the derivative of a field swept 2-pulse electron spin−echo experiment is shown (pulse width 200 ns, pulse separation 400 ns; at T = 20 K 20 echos were accumulated, repetition rate 20/s, at T = 5 K, 64 echos at 5/s. See also text.)

was taken at helium temperatures to avoid saturation of the signal, by reducing the microwave power until the shape of the spectra remained constant (for detailed experimental conditions see caption of Figure 3).

The amplitude of the signal of the biradical generated by chemical reduction increased with increasing pH up to pH 9.5, above which it stayed constant. This is expected from the equilibrium between the biradical $Q_A^{-\bullet}Q_B^{-\bullet}$ and the EPR silent $Q_AQ_B^{=}$ states.[41] Consequently, the biradical was prepared at pH 10.5. The EPR spectrum of the biradical formed by photochemical reduction showed the same general characteristics as that obtained by chemical reduction, but had a small admixture of $Q_A^{-\bullet}$ attributed to the fraction of RCs without a bound Q_B (data not shown). The EPR spectra of $Q_A^{-\bullet}$, $Q_B^{-\bullet}$ and $Q_A^{-\bullet}Q_B^{-\bullet}$ were also measured in samples made with RCs of the HC (M266) mutant,[43] which readily incorporates Zn^{2+} in place of Fe^{2+}. The results were essentially identical to those found for nonmutant RCs and are, therefore, not shown.

From an inspection of Figures 2 and 3 the following main conclusions can be drawn:

(i) The spectrum of $Q_A^{-\bullet}$ (Figure 2a,d,g) is similar to $Q_B^{-\bullet}$ (Figure 2b,e,h), as has been found earlier.[62−65]

(ii) The three peaks in the spectra of $Q_A^{-\bullet}$ and $Q_B^{-\bullet}$ are progressively better resolved with increasing microwave frequency. The resolved peaks are due to the anisotropy of the g-tensor and are labeled g_x, g_y, and g_z in Figure 2g.[63,65]

(iii) The spectra of the biradical $Q_A^{-\bullet}Q_B^{-\bullet}$ (Figure 2c,f,i) deviate significantly from a simple superposition of the $Q_A^{-\bullet}$ and $Q_B^{-\bullet}$ spectra. This shows the presence of a magnetic interaction between $Q_A^{-\bullet}$ and $Q_B^{-\bullet}$.

(iv) The peaks associated with g_x and g_y are split in the biradical spectrum, whereas that associated with g_z remains unsplit (Figure 2i). The peak associated with g_z has a g-factor slightly larger than that for $Q_A^{-\bullet}$ and $Q_B^{-\bullet}$.

(v) The relative amplitudes of the peaks of the biradical are temperature dependent (see Figure 3a,b), whereas those of $Q_A^{-\bullet}$ and $Q_B^{-\bullet}$ are temperature independent (data not shown).

The above findings are addressed and explained in the next sections.

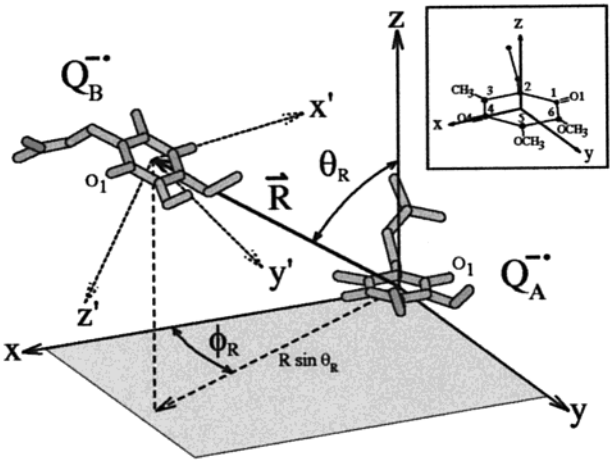

Figure 4. Geometry of the quinone biradical $Q_A^{-\bullet}Q_B^{-\bullet}$. The coordinate axes x, y, z and x', y', z' are along the principal directions of g_A and g_B, respectively, as defined by Isaacson et al.[63] **R** relates the origin of $Q_B^{-\bullet}$ to the origin of $Q_A^{-\bullet}$. θ_R and ϕ_R are the polar and azimuthal angles of **R**. The quinone molecule $Q_A^{-\bullet}$ is shown in the inset. We indicate the position of O1 to emphasize the ∼180° flip of the quinone rings.

Theory

We use a spin Hamiltonian to model the coupled quinone biradical $Q_A^{-\bullet}Q_B^{-\bullet}$, from which the EPR spectra of randomly oriented (frozen solutions) samples of RCs as a function of microwave frequency and temperature were calculated. We describe first the relevant geometric parameters of the biradical, followed by the presentation of the spin Hamiltonian containing the geometric and magnetic parameters. The parameters of the spin Hamiltonian were determined by fitting the model to the experimental data. The magnitude of the exchange interaction and the relationship between the exchange parameter and the electron-transfer rates are discussed in terms of existing theories.

Geometry of the $Q_A^{-\bullet}Q_B^{-\bullet}$ Biradical. The geometry of the biradical is shown in Figure 4 with the inset showing the molecular structure of the quinone molecule, including the principal axes of the g-tensor. The positions of these axes are suggested by the symmetry of the molecule and are supported by EPR data.[63,65] To describe the structure of the biradical, we define a coordinate system ***xyz***, whose origin is at the center of the ring of $Q_A^{-\bullet}$. The axes ***x*** and ***y*** are in the plane of the ring, and the ***z***-axis is normal to it (Figure 4). The second quinone, $Q_B^{-\bullet}$, is related to the first by three elementary rotations given by the Euler angles ϕ_E, θ_E, and ψ_E, which transform the coordinate system ***xyz*** (for $Q_A^{-\bullet}$) to the system ***x′y′z′*** (for $Q_B^{-\bullet}$).

(62) Feher, G. *J. Chem. Soc., Perkin Trans.* **1992**, *2*, 1861−1874.
(63) Isaacson, R. A.; Lendzian, F.; Abresch, E. C.; Lubitz, W.; Feher, G. *Biophys. J.* **1995**, *69*, 311−322.
(64) Feher, G. *Appl. Magn. Reson.* **1998**, *15*, 23−38.
(65) Lubitz, W.; Feher, G. *Appl. Magn. Reson.* **1999**, *17*, 1−48.

As defined by Goldstein;[66] the first rotation (ϕ_E) is applied around the ***z***-axis, the second (θ_E) around the new ***x***-axis, and the third (ψ_E) around the new ***z′***-axis. All rotations are counterclockwise and can have values between 0 and 360°. These rotations are followed by a parallel translation vector, **R**, described by its modulus *R* (the distance between the centers of the two quinone rings) and its polar angles θ_R and ϕ_R in the system of axes ***xyz*** defined by $Q_A^{-\bullet}$. θ_R can vary from 0 to 180° while ϕ_R varies between 0 and 360°. Thus, five angles and one distance define the position of $Q_B^{-\bullet}$ relative to $Q_A^{-\bullet}$. They will be used to describe the magnetic dipolar interaction between $Q_A^{-\bullet}$ and $Q_B^{-\bullet}$.

Spin-Hamiltonian Description of the Biradical. The EPR spectrum of two $S = {}^1/_2$ spins coupled by isotropic and anisotropic interactions has been extensively discussed in textbooks[15,67−69] and in reviews.[70,71] Eaton *et al.* studied the EPR spectra of coupled metal-nitroxyl radical spins in liquid samples considering isotropic *g*-factors, exchange coupling and isotropic hyperfine interaction.[72] They analyzed cases of weakly interacting spins.[73−76] Recently, Hustedt et al. considered pairs of anisotropic nitroxide spin labels coupled by dipolar interactions (but not isotropic exchange), in frozen solutions.[60]

The biradical shown in Figure 4 is formed by the spins on $Q_A^{-\bullet}$ and $Q_B^{-\bullet}$, denoted by $\mathbf{S_A}$ and $\mathbf{S_B}$, respectively, both having $S = {}^1/_2$. They interact with an external magnetic field (Zeeman interaction) and with each other, through exchange and dipole−dipole interactions. The spin-Hamiltonian of this system is

$$H = \mu_B \mathbf{B}\cdot\boldsymbol{g}_\mathbf{A}\cdot\mathbf{S_A} + \mu_B \mathbf{B}\cdot\boldsymbol{g}_\mathbf{B}\cdot\mathbf{S_B} + H_{ex} + H_d \qquad (3)$$

where $\boldsymbol{g}_\mathbf{A}$ and $\boldsymbol{g}_\mathbf{B}$ are the *g*-tensors of $\mathbf{S_A}$ and $\mathbf{S_B}$, and μ_B is the Bohr magneton. The first two terms are the Zeeman interactions of $Q_A^{-\bullet}$ and $Q_B^{-\bullet}$ with the applied magnetic field **B.** Since the principal axes of $\boldsymbol{g}_\mathbf{A}$ and $\boldsymbol{g}_\mathbf{B}$ are related to the molecular axes of $Q_A^{-\bullet}$ and $Q_B^{-\bullet}$ (see inset of Figure 4), the measurement of $\boldsymbol{g}_\mathbf{A}$ and $\boldsymbol{g}_\mathbf{B}$ *in an oriented single-crystal sample* enables one to calculate the orientations (i.e., three Euler angles) of the quinones within the RC.[63] H_{ex} and H_d in eq 3 are, respectively, the isotropic (Heisenberg) exchange and the dipole−dipole interactions that couple $\mathbf{S_A}$ with $\mathbf{S_B}$. The exchange contribution to eq 3 is given by

$$H_{ex} = -J_o\, \mathbf{S_A}\cdot\mathbf{S_B} \qquad (4)$$

where J_o is the exchange parameter defined as the energy splitting between the singlet and triplet spin states.[19,77] The origin of J_o is discussed later in this section. Anisotropic contributions to the exchange interaction are expected to be small,[19] and will not be considered. The dipole−dipole interaction between the quinones can be written as[15,78]

$$H_\mathbf{d} = \frac{1}{R^3}[\mu_\mathbf{A}\cdot\mu_\mathbf{B} - 3(\mu_\mathbf{A}\cdot\boldsymbol{\rho})(\mu_\mathbf{B}\cdot\boldsymbol{\rho})] \approx E_d[\mathbf{S_A}\cdot\mathbf{S_B} - 3(\mathbf{S_A}\cdot\boldsymbol{\rho})(\mathbf{S_B}\cdot\boldsymbol{\rho})], \quad \text{with} \quad E_d = \frac{g^2\mu_B^2}{R^3} \qquad (5)$$

where *R* is the distance between the spins and $\boldsymbol{\rho} = \mathbf{R}/|\mathbf{R}|$ is the unit vector along **R**. The vector $\boldsymbol{\rho}$ in eq 5 introduces an angular variation in H_d. The *g*-values of $\mathbf{S_A}$ and $\mathbf{S_B}$ in eq 5 are assumed equal and isotropic; thus, the average *g*-value is used.

There are two types of contributions to eq 3. One depends on the external magnetic field **B** (Zeeman terms), the other does not (H_{ex} and H_d). The relative magnitudes of the two contributions depend on the applied microwave frequency. The fields applied in the EPR experiments at 9.6, 35 and 94 GHz are 0.343, 1.25 and 3.35 T, respectively. The anisotropies of $\boldsymbol{g}_\mathbf{A}$ and $\boldsymbol{g}_\mathbf{B}$ ($\Delta g/g \approx 0.2\%$) produce at these frequencies maximum shifts of the resonances of $Q_A^{-\bullet}$ and $Q_B^{-\bullet}$ for magnetic field orientations along the g_x and g_z axes of ∼0.65, 2.5, and 6.7 mT, respectively. We shall show later that in the $Q_A^{-\bullet}Q_B^{-\bullet}$ biradical, because of the relative orientation of the quinones, the shifts at 9.6 GHz due to the *g*-anisotropy are smaller than the splitting of the resonance arising from the magnetic interaction between the quinones. However, at 94 GHz the values of the *g*-anisotropy and the magnetic interaction between the quinones are comparable. These changes in condition with frequency help to determine the large number of parameters of the spin Hamiltonian in the multifrequency EPR study presented here.

The spin Hamiltonian of eq 3 contains thirteen independent parameters describing the electronic and geometric structure of the biradical. These parameters, obtained from the experimental data, are:

(i) The *g*-tensors $\boldsymbol{g}_\mathbf{A}$ and $\boldsymbol{g}_\mathbf{B}$. If we refer the problem to the base of eigenvectors of $\boldsymbol{g}_\mathbf{A}$ there are three principal *g*-values for each tensor plus the three Euler angles relating the principal axes of $\boldsymbol{g}_\mathbf{B}$ to the principal axes of $\boldsymbol{g}_\mathbf{A}$ (ϕ_E, θ_E, ψ_E), defined in Figure 4, resulting in a total of nine parameters.

(ii) The magnitude of the isotropic exchange J_o, which provides information about the electronic structure of the path connecting the quinones.

(iii) The magnitude E_d of the dipolar interaction (in eq 5 we use the point dipole approximation) depends on the distance *R*. H_d in eq 5 depends also on the direction of the vector **R** connecting $Q_A^{-\bullet}$ and $Q_B^{-\bullet}$. Thus, the dipolar interaction provides information about the molecular structure (i.e., *R*, θ_R and ϕ_R, see Figure 4).

In addition to these 13 parameters, we have to consider the intrinsic line widths, which could be observed, for instance, in single crystal samples. These line widths arise mainly from unresolved hyperfine interactions of the unpaired electron spin with the surrounding nuclei. We use the same line width for $Q_A^{-\bullet}$ and for $Q_B^{-\bullet}$ in the biradical, and neglect their anisotropy (see section Analysis of the Data). This makes a total of fourteen parameters to be evaluated from the data.

EPR Spectra of the Biradical. Oriented Biradicals. For a given direction $\boldsymbol{h} = \mathbf{B}/|\mathbf{B}|$ of the applied magnetic field, the

(66) Goldstein, H. *Classical Mechanics*, 2nd ed.; Addison-Wesley: Reading, MA, 1980; Chapter 4.4.

(67) Abragam, A.; Bleaney, B. *Electron Paramagnetic Resonance of Transition Ions*; Clarendon Press: Oxford, 1970; Chapter 9.

(68) Bencini, A.; Gatteschi, D. *Electron Paramagnetic Resonance of Exchange Coupled Systems*; Springer: Berlin, 1990; Chapter 3.

(69) Pilbrow, J. R. *Transition Ion Electron Paramagnetic Resonance*; Clarendon: Oxford, 1990; Chapters 5, 7.

(70) Smith, T. D.; Pilbrow, J. R. *Coord. Chem. Rev.* **1974**, *13*, 173−278.

(71) Eaton, G. R.; Eaton, S. S. In *Biological Magnetic Resonance*; Berliner, L. J., Reuben, J., Eds.; Plenum: New York, 1989; Vol. 8, pp 339−396.

(72) In liquid samples, dipolar and other anisotropic contributions are averaged out due to the fast molecular rotation in the liquid.

(73) Eaton, S. S.; DuBois, D. L.; Eaton, G. R. *J. Magn. Reson.* **1978**, *32*, 251−263.

(74) Eaton, S. S.; Eaton, G. R. *Coord. Chem. Rev.* **1978**, *26*, 207−262.

(75) Eaton, S. S.; Eaton, G. R. *J. Am. Chem. Soc.* **1982**, *104*, 5002−5003.

(76) Eaton, S. S.; More, K. M.; Sawant, B. M.; Eaton, G. R. *J. Am. Chem. Soc.* **1983**, *105*, 6560−6567.

(77) There are different definitions of the exchange interaction parameter (see ref 19).

(78) The dipolar parameter E_d of eq 5 is related to the dipolar splitting parameter *D* used in the description of molecular triplet states by $E_d = -2D/3$.

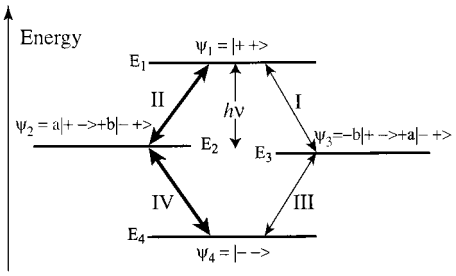

Figure 5. Energy levels (E_1,... E_4) corresponding to wave functions Ψ_1,...Ψ_4, and EPR transitions (I,... IV) for the biradical $Q_A^{-\bullet}Q_B^{-\bullet}$ (see eqs 8−10). Predominant transitions (II and IV, see inset in Figure 6b) are indicated by bold arrows. At low temperatures, levels E_2 and E_3 are less populated than level E_4, leading to intensities of transitions III and IV that are larger than those of transitions I and II. This accounts for the changes in line shape with temperature (see Figure 3).

spin Hamiltonian of eq 3 can be written as[68,73]

$$H = \mu_B B g_A(\boldsymbol{h}) S_{Az} + \mu_B B g_B(\boldsymbol{h}) S_{Bz} - (J_o - d(\boldsymbol{h})) S_{Az} S_{Bz} - {}^1/_2(J_o + {}^1/_2 d(\boldsymbol{h}))(S_{A+}S_{B-} + S_{A-}S_{B+}) + \text{nonsecular terms} \quad (6)$$

where $S_{A+} = S_{Ax} + i\,S_{Ay}$, $S_{A-} = S_{Ax} - iS_{Ay}$, $S_{B+} = S_{Bx} + iS_{By}$ and $S_{B-} = S_{Bx} - iS_{By}$ are spin operators,

$$g_A(\boldsymbol{h}) = (\boldsymbol{h}.\boldsymbol{g_A}.\boldsymbol{g_A}.\boldsymbol{h})^{1/2}; \quad g_B(\boldsymbol{h}) = (\boldsymbol{h}.\boldsymbol{g_B}.\boldsymbol{g_B}.\boldsymbol{h})^{1/2} \quad (7a)$$

and

$$d(\boldsymbol{h}) = E_d(1 - 3\cos^2\eta) \quad (7b)$$

depend on the direction $\boldsymbol{h} = \mathbf{B}/|\mathbf{B}|$ of the applied magnetic field $\mathbf{B}$, and η is the angle between $\boldsymbol{\rho}$ and $\boldsymbol{h}$. The nonsecular terms of the magnetic dipolar interaction connect states having energy splittings of $\sim g\mu_B B$. Their contributions to the energies of the levels are $E_d/(g\mu_B B)$ times smaller than those of the secular contribution E_d, and are, therefore, neglected. With this approximation the eigenvectors Ψ_i and eigenvalues E_i of eq 6 are

$$\Psi_1 = |{+}{+}\rangle \quad \text{with} \quad E_1 = {}^1/_2\mu_B(g_A(\boldsymbol{h}) + g_B(\boldsymbol{h}))B - {}^1/_4(J_o - d(\boldsymbol{h})) \quad (8a)$$

$$\Psi_2 = a|{+}{-}\rangle + b|{-}{+}\rangle \quad \text{with} \quad E_2 = {}^1/_4(J_o - d(\boldsymbol{h})) + {}^1/_2[\mu_B^2(g_A(\boldsymbol{h}) - g_B(\boldsymbol{h}))^2B^2 + (J_o + {}^1/_2 d(\boldsymbol{h}))^2]^{1/2} \quad (8b)$$

$$\Psi_3 = -b|{+}{-}\rangle + a|{-}{+}\rangle \quad \text{with} \quad E_3 = {}^1/_4(J_o - d(\boldsymbol{h})) - {}^1/_2[\mu_B^2(g_A(\boldsymbol{h}) - g_B(\boldsymbol{h}))^2B^2 + (J_o + {}^1/_2 d(\boldsymbol{h}))^2]^{1/2} \quad (8c)$$

$$\Psi_4 = |{-}\,{-}\rangle \quad \text{with} \quad E_4 = -{}^1/_2\mu_B(g_A(\boldsymbol{h}) + g_B(\boldsymbol{h}))B - {}^1/_4(J_o - d(\boldsymbol{h})) \quad (8d)$$

where $a = \cos\alpha$, $b = \sin\alpha$, and

$$\tan\alpha = \frac{-(J_o + {}^1/_2 d(\boldsymbol{h}))}{\mu_B(g_A(\mathbf{h}) - g_B(\mathbf{h}))B + [\mu_B^2(g_A(\boldsymbol{h}) - g_B(\boldsymbol{h}))^2B^2 + (J_o + {}^1/_2 d(\boldsymbol{h}))^2]^{1/2}} \quad (9)$$

There are four allowed EPR transitions between the states Ψ_i, as shown in Figure 5. They are:

I $\Psi_1 \leftrightarrow \Psi_3$, at

$$B_I = B_o + \frac{J_o - d(\boldsymbol{h})}{\mu_B(g_A(\boldsymbol{h}) + g_B(\boldsymbol{h}))} - \frac{[\mu_B^2(g_A(\boldsymbol{h}) - g_B(\boldsymbol{h}))^2B_I^2 + (J_o + {}^1/_2 d(\boldsymbol{h}))^2]^{1/2}}{\mu_B(g_A(\boldsymbol{h}) + g_B(\boldsymbol{h}))} \quad (10a)$$

II $\Psi_1 \leftrightarrow \Psi_2$ at

$$B_{II} = B_o + \frac{J_o - d(\boldsymbol{h})}{\mu_B(g_A(\boldsymbol{h}) + g_B(\boldsymbol{h}))} + \frac{[\mu_B^2(g_A(\boldsymbol{h}) - g_B(\boldsymbol{h}))^2B_{II}^2 + (J_o + {}^1/_2 d(\boldsymbol{h}))^2]^{1/2}}{\mu_B(g_A(\boldsymbol{h}) + g_B(\boldsymbol{h}))} \quad (10b)$$

III $\Psi_3 \leftrightarrow \Psi_4$ at

$$B_{III} = B_o - \frac{J_o - d(\boldsymbol{h})}{\mu_B(g_A(\boldsymbol{h}) + g_B(\boldsymbol{h}))} + \frac{[\mu_B^2(g_A(\boldsymbol{h}) - g_B(\boldsymbol{h}))^2B_{III}^2 + (J_o + {}^1/_2 d(\boldsymbol{h}))^2]^{1/2}}{\mu_B(g_A(\boldsymbol{h}) + g_B(\boldsymbol{h}))} \quad (10c)$$

IV $\Psi_2 \leftrightarrow \Psi_4$ at

$$B_{IV} = B_o - \frac{J_o - d(\boldsymbol{h})}{\mu_B(g_A(\boldsymbol{h}) + g_B(\boldsymbol{h}))} - \frac{[\mu_B^2(g_A(\boldsymbol{h}) - g_B(\boldsymbol{h}))^2B_{IV}^2 + (J_o + {}^1/_2 d(\boldsymbol{h}))^2]^{1/2}}{\mu_B(g_A(\boldsymbol{h}) + g_B(\boldsymbol{h}))} \quad (10d)$$

where $B_o = 2h\nu/[\mu_B(g_A(\boldsymbol{h}) + g_B(\boldsymbol{h}))]$ is the average field of the spectrum for a given orientation $\boldsymbol{h}$. The positions B_i (i = I,..., IV) of the resonances in eqs 10 may be calculated by approximating first $B_i = B_o$, and then iterating the resulting values of B_i until the value obtained on the left side equals the value introduced on the right side.[60,69] The transition probabilities of the resonances of eqs 10 are[69]

$$P_I = P_{III} = |\langle\Psi_1|S_{A+} + S_{B+}|\,\Psi_3\rangle|^2 = 1 - \sin(2\alpha) \quad (11a)$$

$$P_{II} = P_{IV} = |\langle\Psi_1|S_{A+} + S_{B+}|\Psi_2\rangle|^2 = 1 + \sin(2\alpha) \quad (11b)$$

where α, defined in eq 9, depends on the orientation $\boldsymbol{h}$ of the applied magnetic field. Therefore, positions and transition probabilities of these resonances are angular dependent. Their values as a function of $\boldsymbol{h}$ are obtained from eqs 10 and 11.

Equations 10a−d simplify when the dipolar term is negligible (i.e., $E_d = 0$). This corresponds to the familiar two-spin (AB) problem in solution NMR.[79] To gain insight into the effect of the magnetic interaction on the spectrum we consider two limiting cases:

(i) In the low field limit $|(g_A - g_B)\mu_B B| \ll |J_o|$, assuming $E_d = 0$, two transitions occur with a high transition probability (eq 11) at

$$B_o \pm (g_A - g_B)^2\mu_B B_o^2/(2(g_A + g_B)J_o) \quad (12)$$

(79) Poole, C. P. J.; Farach, H. A. *Theory of Magnetic Resonance*, 2nd ed.; Wiley: New York, 1987; Chapters 3−5.

and two transitions occur with a low transition probability at

$$B_o \pm 2J_o/(g_A + g_B)\mu_B \tag{13}$$

For the strong transition (eq 12), a single resonance at B_o is observed when $g_A = g_B$. This resonance splits symmetrically around B_o by $\pm(g_A - g_B)^2\mu_B B_o^2/(2(g_A + g_B)J_o)$ when $g_A \neq g_B$. Thus, when the *g*-factors are similar, the effect of the exchange interaction is small. In the more general case, $E_d \neq 0$, and the low field condition becomes

$$|(g_A - g_B)\mu_B B| \ll |J_o + {}^1/_2 d(\boldsymbol{h})| \tag{14}$$

In this case, tan $\alpha \approx \pm 1$, and sin$(2\alpha) \approx \pm 1$, giving rise to a pair of transitions that have a large transition probability, II and IV when $(J_o + {}^1/_2 d(\boldsymbol{h})) < 0$ and tan $\alpha \approx +1$, or I and III when $(J_o + {}^1/_2 d(\boldsymbol{h})) > 0$ and tan $\alpha \approx -1$ (see eqs 11a,b). The relative intensities of the weaker transitions increase at larger microwave frequencies (i.e., larger B and $|(g_A - g_B)\mu_B B|$).

(ii) In the high field limit $|(g_A - g_B)\mu_B B| \gg |J_o|$, assuming $E_d = 0$, two doublets centered at g_A and g_B appear. Each doublet shows a splitting equal to $J_o/(g\mu_B)$, with the four transitions having similar intensities. Transitions I and IV correspond to a flip of $\mathbf{S_A}$, and transitions II and III to a flip of $\mathbf{S_B}$. This last condition is approximately valid also for the more general case, when $E_d \neq 0$, and $|(g_A - g_B)\mu_B B| \gg |J_o + {}^1/_2 d(\boldsymbol{h})|$ (see eqs 9, 10, and 11).

The two limiting cases considered above, are helpful in understanding qualitatively the spectra of the biradical. However, for a quantitative fitting of the spectra we used eqs 10 a−d without the above-mentioned high field or low field approximations.

Randomly Oriented Biradicals. In a frozen solution (equivalent to a powdered sample), the RCs are immobilized with a random distribution of orientations. The EPR spectra of randomly oriented spins $S = {}^1/_2$ have been discussed in detail.[67,69,80] The important features of the EPR spectra (dχ''/dB) are the peaks arising from molecules having the eigenvectors of the *g*-tensor oriented along the field direction. Thus, different parts of the spectra provide information about molecules with different orientations of the applied magnetic field. In a few cases having high symmetry, the spectra can be calculated analytically. In all other cases they are calculated numerically, as described below.

The spectra observed for the biradical were simulated numerically by summing each of the four resonances (eqs 10 and 11) over all orientations of the applied magnetic field. The sphere containing all possible orientations (θ,ϕ) of the magnetic field B is divided into $(n_\theta \times n_\phi)$ surface elements. Each element subtends a solid angle:

$$\Delta\Omega = 2\pi \sin\theta\, \Delta\theta\, \Delta\phi \tag{15}$$

where $\Delta\theta = \pi/n_\theta$ and $\Delta\phi = \pi/n_\phi$. The amplitude of the spectrum at each magnetic field direction (θ,ϕ) is multiplied by the surface element $\Delta\Omega$ (eq 15) and summed over all field orientations. The values of n_θ and n_ϕ were chosen at each microwave frequency such that a further increase of their values changed the calculated spectrum by an amount smaller than the experimental uncertainty. Typical values of n_θ and n_ϕ were 25, 40, and 80 at 9, 35, and 94 GHz, respectively.

The summation over all molecular orientations in the powder sample requires, in principle, the knowledge of the EPR line width as a function of orientation. However, in view of the large number of parameters we have assumed in our calculations an angular independent (isotropic) line width. Furthermore, the correction proposed by Aasa and Vänngård[80] to account for the difference between frequency and field-swept spectra is very small for our case (less than 0.1%), and was therefore neglected.

Temperature Dependence of the Spectra. The contribution of each resonance (I,.., IV) to the observed spectrum changes with temperature (T) as a consequence of the change in the equilibrium populations of the energy levels E_i ($i = 1, 4$) (see Figure 5). The populations of levels E_2 and E_3 are smaller than that of level E_4 by the Boltzmann factor $\exp(-h\nu/k_B T)$, where ν is the microwave frequency. Thus, when T is lowered, the intensities of the absorptions arising from transitions I and II decrease, while those of transitions III and IV increase. These changes with temperature of the spectrum of the biradical were considered in our calculation. Since the data were normalized, we do not need to consider contributions that change the overall intensity of the signal with temperature, but do not change its line shape. No major spectral shape changes with temperature should be observed for single quinone radicals or for radicals where the coupling is negligible.

Relation of J_o to the Exchange Path. The basic ideas about the origin of the exchange interaction between two spins connected by a diamagnetic bridge were introduced by Anderson,[16] and extended by Zeiger and Pratt,[17] Hay et al.,[18] and Kahn and collaborators.[19] In a simple picture, the electronic Hamiltonian associated with a pair of unpaired electrons 1 and 2 is given by

$$h = h(1) + h(2) + g(1,2) \tag{16}$$

where all electrons except the two unpaired ones are considered as passive. In eq 16,

$$h(\mathrm{i}) = \frac{p_i^2}{2m} - \frac{\mathrm{Ze}^2}{r_{\mathrm{A}i}} - \frac{\mathrm{Ze}^2}{r_{\mathrm{B}i}}, \quad i = 1, 2 \tag{17}$$

is the single electron Hamiltonian for electron i interacting with nuclei at molecules A and B, and

$$g(1,2) = \frac{e^2}{|r_1 - r_2|} \tag{18}$$

is the inter-electronic Coulomb repulsion between the two electrons. Two orbitals, φ_A and φ_B (sometimes called magnetic orbitals), centered on A and B, respectively, occupied by a single electron delocalized through the surrounding ligands, are the eigenfunction of the one-electron local Hamiltonian. The parameters of the EPR spectra of A or B (*g*-shifts, anisotropies, etc) could, in principle, be derived from the expression of the orbitals φ_A and φ_B, respectively. The linear combinations

$$\varphi_{\pm}^{(\mathrm{gc})} = \frac{1}{2^{1/2}}[\varphi_A(1)\varphi_B(2) \pm \varphi_A(2)\varphi_B(1)] \tag{19}$$

would be, in the absence of an interaction, the orbital wave functions associated with the singlet and triplet states obtained for the two electrons in the ground-state configuration (gc). When the interaction is strong the appropriate orbitals have to be modified. However, when the interaction is weak, the functions of eq 19 represent a first-order approximation describing these states. There are two additional states in the excited charge-transfer configuration (ec) with two electrons on A, or two electrons on B, and with energy U above the ground

(80) Aasa, R.; Vänngård, T. *J. Magn. Reson.* **1975**, *19*, 308−315.

configuration $\varphi_{\pm}^{(ec)}$, which may be described by

$$\varphi_{\pm}^{(ec)} = \frac{1}{2^{1/2}}[\varphi_A(1)\varphi_A(2) \pm \varphi_B(1)\varphi_B(2)] \qquad (20)$$

and represent the two singlet states of the excited configuration. The state $\varphi_{\pm}^{(gc)}$ is mixed with the excited state $\varphi_{\pm}^{(ec)}$, producing the splitting of the two ground-state orbitals that gives rise to the exchange interaction J_o. In Anderson's theory, J_o is given by[16,17,19,81]

$$J_o = 2k - \frac{(\beta + l)^2}{U} \qquad (21)$$

where,

$$\beta = \langle\varphi_A(1)|h(1)|\ \varphi_B(1)\rangle,$$
$$k = \langle\varphi_A(1)\varphi_B(2)|g(1,2)|\varphi_A(2)\varphi_B(1)\rangle, \quad \text{and}$$
$$l = \langle\varphi_A(1)\varphi_B(2)|g(1,2)|\varphi_B(1)\varphi_B(2)\rangle \qquad (22)$$

are the transfer, exchange and ionic integrals, respectively. The exchange integral $k > 0$, and gives rise to a ferromagnetic contribution to J_o. For large distances, R, between spins, k and l are small[16−19] and J_o can be approximated by

$$J_o \approx -\beta^2/U \qquad (23)$$

where the perturbative calculation leading to eqs 21, 22, and 23 assumes $|\beta| \ll U$. Equation 23 allows us to relate the experimental value of J_o to the integral $\beta = \langle\varphi_A(1)|h(1)|\ \varphi_B(1)\rangle$, which depends on the exchange path, and on the energy difference U. This result is used below to estimate the electron-transfer rate between the semiquinones $Q_A^{-\bullet}$ and $Q_B^{-\bullet}$, in the photosynthetic reaction center.

Relation of the Electron-Transfer Rate to J_o. The electron-transfer rate, k_{ET}, can be described by the Marcus theory:[82,83]

$$k_{ET} = \frac{2\pi|V_{if}|^2}{\hbar}F \qquad (24)$$

$$F = \frac{1}{\sqrt{4\pi\lambda k_B T}}\exp\left[-\frac{(\Delta G_{ET} + \lambda)^2}{4\lambda k_B T}\right] \qquad (25)$$

where V_{if} is the electronic matrix element coupling the initial (i) and final (f) states, and F is the Franck−Condon term, with λ the reorganization energy, ΔG_{ET} the redox free energy for the reaction, k_B the Boltzmann constant, and T the temperature. The exponential in the Franck−Condon term is maximum for $\Delta G_{ET} = -\lambda$. For this case the maximum rate $(k_{ET})^{max}$ is given by[84−86]

$$(k_{ET})^{max} = \frac{2\pi|V_{if}|^2}{\hbar\sqrt{4\pi\lambda k_B T}} \qquad (26)$$

If the magnetic orbitals introduced before (eqs 19−20) and the electronic orbitals for the electron transfer reaction are the same, one can quantitatively relate J_o to the matrix element V_{if} for the reaction $A^{-\bullet}B^{-\bullet} \rightarrow AB^{=}$.[34] To show this, we briefly describe a model for the electron-transfer reaction.[83,87,88]

Within the Born−Oppenheimer approximation the wave functions describing the two states $A^{-\bullet}$ and $B^{-\bullet}$ can be written as

$$\Psi_A = \chi_A(q)\varphi_A(r,q),\ \Psi_B = \chi_B(q)\varphi_B(r,q) \qquad (27)$$

respectively. χ_A and χ_B in eq 27 represent the vibrational parts, and φ_A and φ_B the electronic parts. All of them depend on the nuclear coordinates q. Within our approximation, φ_A and φ_B are the same functions used in the description of the exchange interaction J_o. The wave functions Ψ_A and Ψ_B (eq 27) are not stationary; the time-dependent state may be written as

$$\Psi(r,q,t) = \chi_A(q,t)\ \varphi_A(r,q) + \chi_B(q,t)\ \varphi_B(r,q) \qquad (28)$$

where $\chi_A(q,t)$ and $\chi_B(q,t)$ can be determined using the time-dependent Schrödinger equation:

$$h\Psi = i\hbar\frac{\partial\Psi}{\partial t} \qquad (29)$$

where h is defined in eq 16, and the initial conditions are

$$\chi_A(q,0) = \chi_A(q) \quad \text{and} \quad \chi_B(q,0) = 0 \qquad (30)$$

Equations 27−30 allow to calculate the matrix elements V_{if} of eqs 24 and 26 as[87,88]

$$V_{if} = \beta_{ET} + T_{AB}' + T_{AB}'' \qquad (31)$$

where

$$\beta_{ET} = \langle\varphi_A(r,q)|h(1)|\varphi_B(r,q)\rangle,$$
$$T_{AB}' = -\sum_k \frac{\hbar^2}{M_k}\langle\varphi_A||\partial\varphi_B/\partial q_k\rangle\,\partial/\partial q_k,$$
$$T_{AB}'' = -\sum_k \frac{\hbar^2}{2M_k}\langle\varphi_A||\partial^2\varphi_B/\partial q_k 2\rangle \qquad (32)$$

The contributions T_{AB}' and T_{AB}'' (eqs 31 and 32), which take into account the kinetics of the nuclear coordinates, are smaller than β_{ET}, and will be neglected. This arises from applying the Born−Oppenheimer approximation to the problem, and has been discussed in detail by several authors.[82,87−89] Thus, $V_{if} \approx \beta_{ET} \approx \beta$, which is related to J_o by eq 23, or

$$|V_{if}|^2 \approx (\beta_{ET})^2 \approx \beta^2 \approx U|J_o| \qquad (33)$$

Equation 33 allows one to estimate the matrix element of the electron-transfer reaction from the value of the exchange parameter J_o. Specifically, it relates the magnitude J_o of the exchange interaction between $A^{-\bullet}$ and $B^{-\bullet}$, to the tunneling matrix elements for the reaction $A^{-\bullet}B^{-\bullet} \rightarrow AB^{=}$.[34] The justification of eq 33 is that the pathway connecting the two

(81) Girerd, J. J.; Jornaux, Y.; Kahn, O. *Chem. Phys. Lett.* **1981**, *82*, 534−538.
(82) DeVault, D. *Quantum Mechanical Tunneling in Biological Systems*; Cambridge University Press: Cambridge, 1984; Chapter 5.
(83) Marcus, R. A.; Sutin, N. *Biochim. Biophys. Acta* **1985**, *811*, 265−322.
(84) Moser, C. C.; Keske, J. M.; Warncke, K.; Farid, R. S.; Dutton, P. L. *Nature* **1992**, *355*, 796−802.
(85) Dutton, P. L.; Moser, C. C. *Proc. Natl. Acad. Sci. U.S.A.* **1994**, *91*, 10247−10250.
(86) Moser, C. C.; Page, C. C.; Farid, R.; Dutton, P. L. *J. Bioenerg. Biomembr.* **1995**, *27*, 263−274.
(87) Newton, M. D.; Sutin, N. *Annu. Rev. Phys. Chem.* **1984**, *35*, 437−480.
(88) Bertrand, P. *Struct. Bonding* **1991**, *75*, 3−47.
(89) O'Malley, T. F. In *Advances in Atomic and Molecular Physics*; Bates, D. R., Esterman, I., Eds.; Academic Press: London, 1971; Vol. 7, pp 223−249.

cofactors in the magnetic coupling is the same as for the electron-transfer process, that is, $\beta_{ET} = \beta$. One neglects the changes of the integral β with the nuclear coordinates, that is, we neglect possible changes in coordinates upon reduction of the quinones. In eq 33, the splitting U between ground and excited configuration can be estimated as[34]

$$U \approx \lambda + \Delta G_{ET} \tag{34}$$

where λ is the reorganization energy and ΔG_{ET} is the free energy difference for the reaction.

Analysis of the Data

Initial Values and Ranges of Values of the Parameters. To reduce the computation time, we estimated the initial values of the parameters and their ranges. The initial value $E_d/h \approx 10$ MHz ($E_d/(g\mu_B) \approx 3.57 \times 10^{-4}$ T)[90] was obtained from the point dipole approximation (eq 5) using the structural result, $R \approx (17.4 \pm 0.3)$ Å.[13] The sign of E_d is by definition positive; the value of E_d was varied within a range of ±50% around the initial value.

For J_o/h we started with a value of zero. No a priori requirement was made on the sign of J_o, which was allowed to take negative and positive values within a wide range (±150 MHz).

The Euler angles (ϕ_E, θ_E, ψ_E) were allowed to vary in ranges of ±60° around the structural values,[13] $\phi_E = 14°$, $\theta_E = 155°$ and $\psi_E = 179°$. The angles defining the orientation of **R**, θ_R and ϕ_R, were allowed to vary ±60° around their crystallographic values (60° and 9°, respectively).

The values of the *g*-factors measured for the individual quinones at 94 GHz (Figure 2g,h) were taken as initial values for the calculation. These values are, within experimental error, in agreement with the values obtained by Isaacson et al.[63] in single-crystal samples at 35 GHz. A range of variation of ±0.0003 was found to be sufficient in all cases.

Another parameter required to fit the data is the EPR line width ΔB of $Q_A^{-\bullet}$ and $Q_B^{-\bullet}$ in the biradical. ΔB is the peak-to-peak line width of $d\chi''/dB$ in an oriented sample. The single crystal work at 35 GHz[63] showed that the line width along the three principal crystallographic directions varied by less than 5% ($\Delta B = (0.41 \pm 0.02)$ mT), which justifies the neglect of the anisotropy. The EPR spectra of $Q_A^{-\bullet}$ and $Q_B^{-\bullet}$ at 94 GHz (Figure 2g,h) could also be fitted with the same values. For the biradical the line width ΔB was assumed to be constant over the spectrum, and the same for the two radicals. However, the value of ΔB was allowed to be different from those of the individual quinones, and considered as a parameter to be obtained from the fit. The starting value was 0.41 mT, as observed for the individual semiquinones.

Fitting of the Data by the Simulated Annealing Method. The values of the magnetic and geometric parameters of the spin Hamiltonian of the biradical were obtained from a simultaneous fit of the six EPR spectra at 35 and 94 GHz shown in Figure 3, as discussed in the Theory section. The data at 9.6 GHz, having a considerably lower resolution than those at the higher frequencies, were not included in the global fitting. To determine the reliability of the simulated annealing method, we performed annealing processes using two different protocols. In the first, we started from different initial sets of parameters, leaving the fitting to evolve to a final value while decreasing T_σ. In the second protocol, we started from the same set of parameters, but chose a different sequence of random numbers. In both cases, we obtained similar final values when we started from a sufficiently high "*temperature*", with a slow "*cooling rate*". In each run, the value of T_σ was reduced by a factor of ~0.3% after each cycle of change of all parameters. Slower reductions of T_σ did not change the results. The number of iterations (total number of simulations for different sets of parameters) of each process was greater than 20000. Each annealing process was stopped when, after ~1000 simulations, no further decrease of $\sigma(p_\alpha)$ occurred.

The values of the parameters of the spin Hamiltonian of the biradical $Q_A^{-\bullet}Q_B^{-\bullet}$ obtained (Tables1 and 2) are the averages of 22 independent runs using the second protocol described above. They are compared to those for $Q_A^{-\bullet}$ and $Q_B^{-\bullet}$ and to the values obtained from the X-ray structure.[13] The root-mean-square deviation (eq 2) of these global fits are $\sigma \approx 2.3\%$. The line width which optimizes the fit is $\Delta B = 0.33$ mT.

In Figure 6a and b we compare the experimental results at 80 K (solid lines) at Q-band and W-band, with the simulations (dotted lines) obtained with the parameters obtained from the global fit (Tables 1 and 2). The simulated EPR spectra are composed of the four transitions shown in Figure 5. Their individual contributions are shown in the insets of Figure 6. The largest contributions to the spectra arise from transitions II and IV (as a consequence of the negative value of J_o).

Table 1. Magnetic Parameters for the Biradical $Q_A^{-\bullet}Q_B^{-\bullet}$ and for the Individual Semiquinones $Q_A^{-\bullet}$ and $Q_B^{-\bullet}$[a]

parameter[b]	$(Q_A^{-\bullet}Q_B^{-\bullet})$[c]	semiquinones[d]
J_o/h (MHz)	-60 ± 20	N. A.[e]
E_d/h (MHz)	10.3 ± 0.1	N. A.[e]
$^1/_2(g_{xA}+g_{xB})$	2.00635(5)	2.00637(5)
$^1/_2\lvert g_{xA}-g_{x'B}\rvert$	$(0 \pm 5) \times 10^{-5}$	$(10 \pm 5) \times 10^{-5}$
$^1/_2(g_{yA}+g_{yB})$	2.00517 (5)	2.00531(5)
$^1/_2\lvert g_{yA}-g_{y'B}\rvert$	$(0 \pm 5) \times 10^{-5}$	$(1 \pm 5) \times 10^{-5}$
$^1/_2(g_{zA}+g_{zB})$	2.00225(5)	2.00215(5)
$^1/_2\lvert g_{zA}-g_{z'B}\rvert$	$(10 \pm 5) \times 10^{-5}$	$(0 \pm 5) \times 10^{-5}$

[a] Numbers in parentheses for $^1/_2(g_{iA}+g_{iB})$ values indicate the error in the last decimal place. [b] We cannot assign specific *g*-values to either $Q_A^{-\bullet}$ or $Q_B^{-\bullet}$ in the high field region (g_z-region in Figure 2g) because the splitting of the spectra due to J_o depends on $(g_A - g_B)^2$ (see eq 12) and the splitting of the spectra due to E_d is negligible, since we are close to the magic angle. For this reason we quote in Table 1 only the absolute values of the differences $|g_{iA} - g_{iB}|$. [c] The parameters for the biradical were obtained from a global fit of the six EPR spectra at 35 and 94 GHz at different temperatures shown in Figure 3, with a line width $\Delta B = 0.33$ mT for $Q_A^{-\bullet}$ and $Q_B^{-\bullet}$ in the biradical. The error is estimated as the standard deviation of the parameters calculated from 22 independent global fits of the data. [d] *g*-values from the 94 GHz results for the semiquinones $Q_A^{-\bullet}$ and $Q_B^{-\bullet}$ in singly reduced RCs (Figure 2g,h). These values are similar to those observed at 35 GHz.[63] [e] Not applicable.

Table 2. Geometric Parameters for the Biradical $Q_A^{-\bullet}Q_B^{-\bullet}$ Obtained from EPR, and from the X-ray Structure[13]

angle	EPR $(Q_A^{-\bullet}Q_B^{-\bullet})$[a]	X-ray structure[b]
R [Å]	17.2 ± 0.2	17.4 ± 0.3
ϕ_E [deg]	21 ± 14	14 ± 7
θ_E [deg]	190 ± 16	155 ± 7
ψ_E [deg]	197 ± 20	179 ± 7
θ_R [deg]	65.6 ± 3.5	60 ± 7
ϕ_R [deg]	2 ± 6	9 ± 7

[a] Values obtained from the global fit of the six spectra at 35 and 94 GHz and different temperatures shown in Figure 3 with a line width $\Delta B = 0.33$ mT for $Q_A^{-\bullet}$ and $Q_B^{-\bullet}$ in the biradical. The errors are the standard deviation of the values obtained from 22 independent global fits of the data. [b] Values obtained from the X-rays structure,[13] averaged over the two molecules in the unit cell.

(90) The Zeeman energy of a spin $^1/_2$ with $g = 2$ in a field of 10^{-4} T is $E/k_B = 1.343 \times 10^{-4}$ K; $E/h = 2.799$ MHz; $E/e = 1.158 \times 10^{-8}$ eV or $E/(hc) = 0.9337 \times 10^{-4}$cm^{-1}.

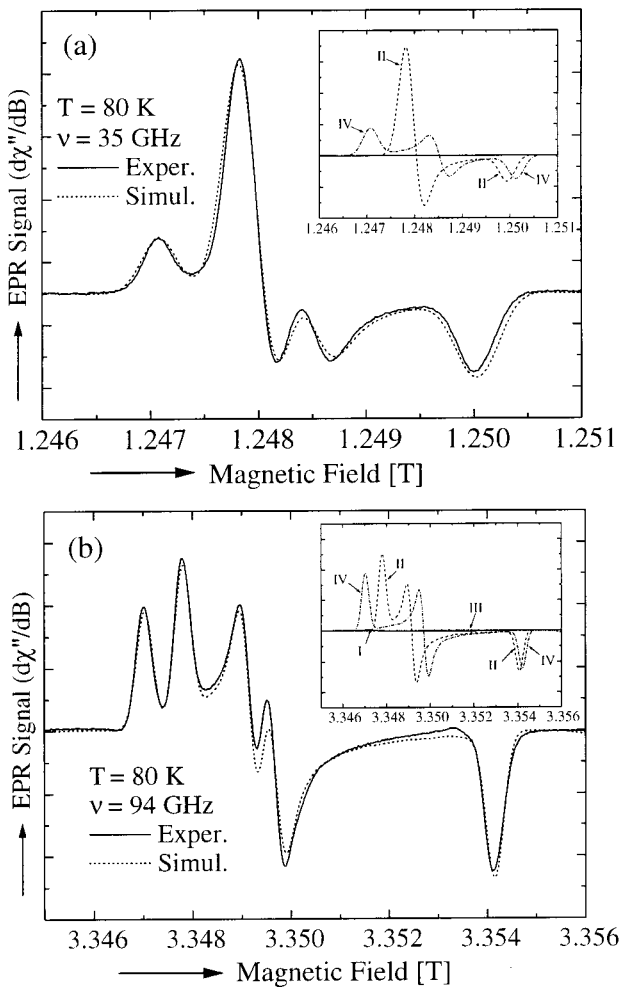

Figure 6. EPR spectra of the biradical $Q_A^{-\bullet}Q_B^{-\bullet}$ at 35 GHz (a) and 94 GHz (b). The experimental results are shown by solid lines and the simulations with the parameters in Tables 1 and 2, obtained from the global fit, are shown by dotted lines. The insets display the calculated contributions of the transitions I, II, III and IV (Figure 5) to the simulated spectra. At 35 GHz the contributions of transitions I and III are not discernible. At 94 GHz they are barely discernible near the baseline.

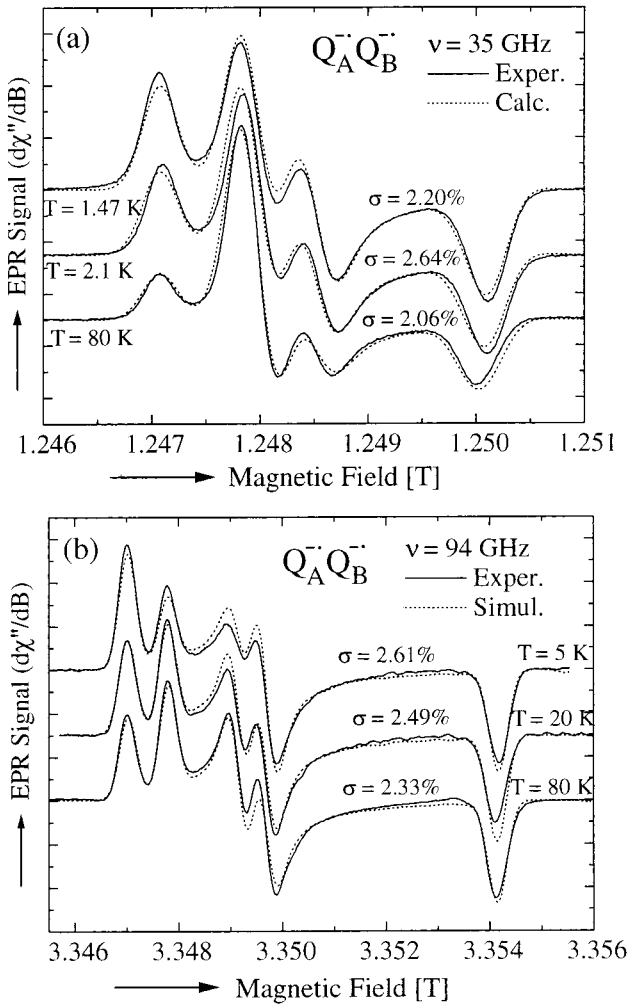

Figure 7. Comparison of the experimental spectra (solid lines) of the biradical $Q_A^{-\bullet}Q_B^{-\bullet}$ with the simulated spectra (dotted line) obtained with the parameters given in Tables 1 and 2, at 35 GHz (a) and 94 GHz (b) for different temperatures. The root-mean-square deviation σ (eq 2) of each spectrum is shown.

Transitions I and III are weak and at 35 GHz they merge with the baseline. At 94 GHz they are barely discernible.

Parts a and b of Figure 7 show the observed (solid lines) and simulated (dotted lines) spectra at 35 and 94 GHz, at different temperatures, calculated with the parameters in Tables 1 and 2. We include in these figures the values of σ obtained for each particular spectrum. The global σ (2.3%) is the average of the individual σ's, weighted by the number of points of each spectrum.

The estimated uncertainties of the spin-Hamiltonian parameters included in Tables 1 and 2 are the standard deviations of 22 global annealing runs performed with the same data, but with different sequences of random numbers.

There is a striking difference between the uncertainties in the value of J_o, compared with E_d. The cause of this difference is illustrated by Figure 8a,b, where the value of the global root-mean-square deviation σ, is plotted against E_d and J_o. For the variation of σ vs E_d (Figure 8a), a well-defined deep minimum is observed. In contrast, the variation of σ vs J_o shows a shallow, poorly defined minimum (Figure 8b). This is because the EPR spectra are not very sensitive to the value of J_o, as discussed in the Theory section. Consequently, J_o has a larger uncertainty. However, Figure 8b leaves little doubt about $J_o < 0$, that is, the exchange interaction between the spins on $Q_A^{-\bullet}$ and $Q_B^{-\bullet}$ is antiferromagnetic.

The uncertainties in the values of some of the parameters (J_o and the Euler angles) given in Tables 1 and 2 are large. They are primarily due to the weak dependence of the simulated powder spectra on these parameters, and to large cross-correlations between pairs of parameters that generate multiple close lying minima of σ in the multidimensional parameters space. Calculation of the cross-correlations between sets of values of the 14 parameters obtained from a very large set of different fitting processes would be too time-consuming to be practical at present. Thus, we constructed histograms of the values obtained for each parameter from the set of 22 global annealing runs performed with the same initial values and calculated the standard deviation of each parameter.

In an independent attempt to clarify the source of the uncertainties, we individually fitted eight independent spectra (at four different temperatures, at 35 and 94 GHz). The root-mean-square deviations of most of the parameters obtained from these individual fits were found to be approximately the same as those obtained from the 22 global fittings. This supports the hypothesis that the main source of errors of these parameters arises from the characteristics of the problem, and not from the experimental uncertainty of the spectra. For example, since the

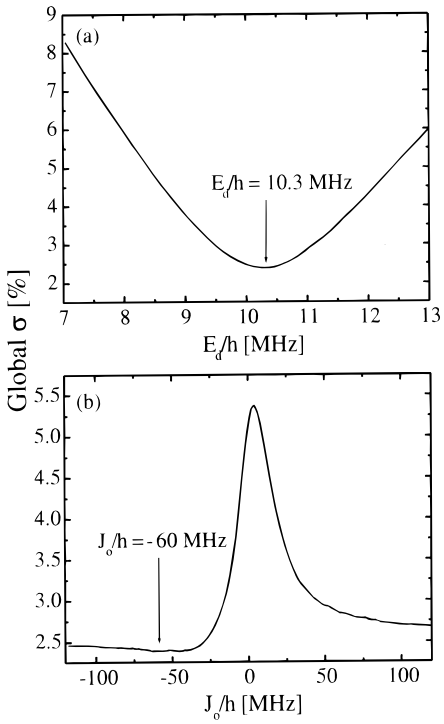

Figure 8. Sensitivity of the global root-mean-square deviation, σ (Eq. 2), to the change of one parameter, when the others are kept constant. (a) σ vs E_d. (b) σ vs J_o. The best values are indicated by arrows. The shallow minimum of J_o (as compared with E_d) results in the relatively large uncertainty in the value of J_o.

angle θ_E is close to 180°, ϕ_E and ψ_E are strongly cross-correlated, since they correspond to rotations in opposite directions around nearly collinear axes. Because of that, we observe that the standard deviation of the values of $\phi_E - \psi_E$ obtained from the 22 global annealings, or from the annealings of eight different spectra, is half of those of the individual standard deviations of ϕ_E and ψ_E.

Although the values of g_x, g_y, and g_z for $Q_A^{-\bullet}$ and $Q_B^{-\bullet}$ determined from the fit of the biradical spectra are very similar to those obtained for independent $Q_A^{-\bullet}$ and $Q_B^{-\bullet}$, they are not identical (see Table 1). We performed a global fitting of the spectra of the biradical fixing the *g*-values to those of the independent semiquinones, shown in Table 1, to determine if these differences are significant. The fit to the data is nearly as good as that described above, with a value of σ that is 10−15% larger. All angles and E_d were the same within uncertainties to those reported in Tables 1 and 2. However, the absolute value of J_o increased to ∼100 MHz and exhibited a shallower minimum.

Discussion

Characterization of the $Q_A^{-\bullet}Q_B^{-\bullet}$ Biradical. The intermediate $Q_A^{-\bullet}Q_B^{-\bullet}$ state of the photocycle of RCs was produced by chemical reduction and by light reduction. The EPR spectra of biradical samples made by the two methods gave essentially the same results. The intensities of the spectra of the biradical produced by chemical reduction showed a pH dependence as expected for the $Q_AQ_B^{=} \rightleftarrows Q_A^{-\bullet}Q_B^{-\bullet}$ equilibrium.[41] Since the chemical method yielded a purer biradical state than the light induced one, we present in this work only EPR data obtained from the chemically produced biradical. We have studied the biradical $Q_A^{-\bullet}Q_B^{-\bullet}$ in RCs of *Rb. sphaeroides* R26 and also in RCs of the HC(M266) mutant.[43] The results are similar; we present, therefore, only the information obtained for *Rb. sphaeroides* R26, for which crystallographic data exist.[13]

General Characteristics of the EPR Spectra and Fit with a Theoretical Model. The experimental data at three frequencies (Figure 2a−i) show that the spectrum of the biradical is not simply a superposition of spectra of the individual radicals. This indicates the existence of a magnetic interaction between $Q_A^{-\bullet}$ and $Q_B^{-\bullet}$ in the $Q_A^{-\bullet}Q_B^{-\bullet}$ biradical state. The spin of each radical, $Q_A^{-\bullet}$ and $Q_B^{-\bullet}$, exert a magnetic field on the other radical that results in a change of the EPR spectrum. We proposed for the biradical a spin Hamiltonian that considers the anisotropic Zeeman interactions with the external magnetic field and isotropic (exchange) and anisotropic (dipole−dipole) interaction terms between the spins of the radicals. From a simultaneous (global) fit of the EPR spectra at 35 and 94 GHz at different temperatures (see Figure 3), we obtained a set of parameters of the spin Hamiltonian given in Tables 1 and 2. The agreement between the observed and the simulated spectra at 35 and 94 GHz obtained with the same set of spin Hamiltonian parameters is very good (see Figures 6a,b, 7a,b). For our case eq 14 applies and $J_o < 0$ (see section Fitting of the Data by...), making transitions II and IV (see Figure 5) the main contributors to the spectra at both frequencies (see eqs 11a and 11b). The relative contributions of transitions I and III increase at higher frequencies (see the insets of parts a and b of Figure 6). At low temperatures the relative contribution of transition IV increases at the expense of transition II, (see eqs 8a−d, Figure 5 and insets of Figure 6). The observed temperature dependence of the spectra at 35 and 94 GHz is reproduced very well by the simulations obtained with the parameters calculated from the global fit of the data (see Figure 7a,b).

In view of the small difference between g_A and g_B, the contribution of the exchange interaction to the observed line shifts of the spectra of the biradical is small (eqs 12 and 14). Therefore, a larger uncertainty was found for the value of J_o than for the value of E_d.

The principal *g*-values calculated from the spectra of the biradical are close to those measured for the individual quinone radicals at 35 GHz[63] and in this work at 94 GHz (see Table 1).

We conclude this section with a brief discussion of a striking feature of the spectra: the absence of a splitting of the high field peak corresponding to g_z, in contrast to the splittings observed for the peaks corresponding to g_x and g_y. The splitting of the peaks is due to both, exchange and dipolar interactions. The dipolar contribution to the splitting is small when the angle between the vector connecting the centers of the quinone rings and the applied magnetic field is near the "magic angle" $\eta = 54.7°$ (see eq 7). Thus, when the magnetic field is along the ***z***-axis of $Q_A^{-\bullet}$, θ_R should be approximately equal to η, or to $180 - \eta$. The results of our calculation showed that θ_R is indeed close to the magic angle. In addition, to account for the lack of splitting of the g_z peak, the contribution of the exchange interaction must also be small at this orientation. This would occur when J_o is negligible or when both quinones have the same *g*-factor (see eq 12). The possibility of a negligible value of J_o was discarded since the results of the computations showed that $|J_o| > E_d$. Consequently, the *g*-values of both radicals along the *z*-axis must be close to each other. Since the ***z***-directions are along the normals to the quinone ring planes, the *g*-factors are equal when the ring planes are parallel (i.e., $\theta_E \approx 0°$ or 180°). The X-rays structure shows that this is, indeed, approximately the case ($\theta_E = 155°$, see Table 2).

Structural Information Obtained from the Dipolar Interaction. Comparison with the X-ray Structure. The pa-

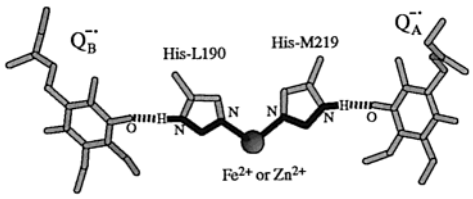

Figure 9. Shortest exchange path connecting $Q_A^{-\bullet}$ with $Q_B^{-\bullet}$. This path is composed of six high electron density bonds, two within each histidine ring, and two connecting the metal ion to the histidines (bold segments), and two low electron density, N−H···O hydrogen bonds (bold, dashed segments). In the RCs used in this work, the Fe^{2+} was replaced by Zn^{2+}.

rameters of the dipolar interaction provide structural information about the $Q_A^{-\bullet}Q_B^{-\bullet}$ biradical (Table 2). The Euler angles relating the axes of the quinones calculated from the EPR spectra of the biradical and the length and orientation of the vector **R** connecting the center of the two quinone molecules are compared with those obtained from the X-ray structure of the $Q_AQ_B^{-\bullet}$ state of the RC of *Rb. sphaeroides.*[13] In the structure of the RC reported by these authors there are two RC molecules in the asymmetric unit cell of the crystal. We obtained the values of the angles and distances for each molecule from the crystallographic data, using the transformation matrix for the Euler angles given by Goldstein,[66] and the average values are given in Table 2. The uncertainties of these values were estimated using the "rule of thumb" that the error in the position of an atom for a refined structure is, on the average, one tenth of the resolution at which the structure was solved.[91] Since the Stowell structure ($Q_AQ_B^{-\bullet}$) was solved to a resolution of 2.6 Å, the uncertainty in the coordinates is ∼0.3 Å. These coordinate errors translate into angular orientation errors of ∼7°.

The distance R of 17.2 Å between the centers of the quinone rings, estimated using the point dipole approximation (eq 5), is the same within the uncertainties (∼0.2 Å) as that observed in the X-ray structure.

The polar and azimuthal angles (θ_R and ϕ_R) of the vector **R** (see Figure 4) do not change from those reported by Stowell et al.[13] Since θ_R and ϕ_R are the same as the crystallographic values, $Q_A^{-\bullet}$ does not rotate upon reduction. Furthermore, since the magnitude of R remains constant, $Q_B^{-\bullet}$ does not move relative to $Q_A^{-\bullet}$. The only difference between the two structures is the angle θ_E that involves a relative rotation of the quinone planes that makes these planes nearly parallel in the biradical state $Q_A^{-\bullet}Q_B^{-\bullet}$. This may indicate a change in the orientation of $Q_B^{-\bullet}$ produced by the electrostatic interaction between $Q_A^{-\bullet}$ and $Q_B^{-\bullet}$.

Magnitude of the Exchange Interaction and its Effect on the Line Width. The experimentally determined exchange interaction, $J_o/h = (-60 \pm 20)$ MHz ($J_o/k_B = (-2.9 \pm 0.9) \times 10^{-3}$ K) is related to the chemical path connecting $Q_A^{-\bullet}Q_B^{-\bullet}$. The shortest path, consisting of six high electron density bonds and two low electron density (hydrogen) bonds is shown in Figure 9.

Hoffmann et al.,[92] extending the results of Coffman and Buettner,[93] proposed a maximum value and an empirical range for J_o as a function of the distance between the unpaired spins. For a distance of 17.2 Å, they predict a range 20 MHz $< |J_o|/h <$ 2000 MHz. The observed value of $|J_o|$ for the $Q_A^{-\bullet}Q_B^{-\bullet}$ biradical is at the lower end of the range, presumably because of the two low electron density (hydrogen) bonds.

The global fit of the EPR spectra at 35 and 94 GHz indicates a reduction of ∼20% of the line width of the biradical ($\Delta B = (0.33 \pm 0.02)$ mT), compared with the line widths of the individual semiquinones ($\Delta B = 0.41 \pm 0.02$) mT). This narrowing is due to the exchange interaction between the two semiquinones. To understand this effect, consider the simple system of an electron with $S = {}^1/_2$ interacting with a nuclear spin $I = {}^1/_2$ (proton). The EPR line is split by the hyperfine interaction A. When two such systems are coupled by an exchange interaction $|J_o| > |A|$, three hyperfine components with relative intensities 1:3:1 and splittings $A/2$ are obtained. This effect was observed many years ago in the EPR spectra of interacting donors in silicon,[94] the theory of which was worked out by Slichter.[95] In the biradical $Q_A^{-\bullet}Q_B^{-\bullet}$ the line width arises from unresolved hyperfine interactions, each of them being smaller than $|J_o|$. We calculated a reduction of ∼40% of the observed line width for the coupled $S = {}^1/_2$, $I = {}^1/_2$ system described above assuming that the hyperfine interaction is larger than the intrinsic line width. When this condition is not satisfied, the narrowing is smaller. Thus, our observed narrowing of 20% in the biradical corresponds to an intermediate case where the hyperfine interaction is comparable to the intrinsic line width.[96] This narrowing provides independent evidence that $|J_o| > |A|$. The narrowing described above is reminiscent of the narrowing observed in the bacteriochlorophyll dimer of the reaction center,[97] although the detailed mechanism for this case is different.[98−100]

Exchange Interaction and Electron-Transfer Rate. The value of the exchange interaction J_o between the semiquinones can be used to estimate the tunneling matrix element V_{if} (see eqs 33 and 34). The mechanism for the second electron reduction of Q_B involves fast reversible protonation of the semiquinone (at rate k_{H^+}), followed by rate-limiting electron transfer, k_{ET}:[101]

$$Q_A^{-\bullet}Q_B^{-\bullet} + H^+ \underset{}{\overset{k_{H^+}}{\rightleftharpoons}} Q_A^{-\bullet}(Q_BH)^{\bullet} \xrightarrow{k_{ET}} Q_A(Q_BH)^- \qquad (35)$$
$$\xrightarrow{\qquad\qquad k_{AB}^{(2)} \qquad\qquad}$$

Since the pathway connecting the two semiquinones (from the carbonyl oxygen of Q_A, through the metal−His complex, to the carbonyl oxygen of Q_B, see Figure 9) should be essentially the same for $Q_A^{-\bullet}(Q_BH)^{\bullet}$ as for $Q_A^{-\bullet}Q_B^{-\bullet}$, we will assume that the same value of J_o, obtained for the biradical in this work, applies to the electron-transfer step of eq 35. With this approximation, and using the values, $\lambda = 1.2$ eV[102,103] and $\Delta G_{ET} = -0.25$ eV,[35] the tunneling matrix element is estimated from

(91) Rhodes, G. *Crystallography Made Crystal Clear: A Guide for Users of Macromolecular Models*; Academic Press: San Diego, 1993; Chapter 8B.

(92) Hoffmann, S. K.; Hilczer, W.; Goslar, J. *Appl. Magn. Reson.* **1994**, *7*, 289−321.

(93) Coffman, R. E.; Buettner, G. R. *J. Phys. Chem.* **1979**, *83*, 2387−2392.

(94) Feher, G.; Fletcher, R. C.; Gere, E. A. *Phys. Rev.* **1955**, *100*, 1784−1786.

(95) Slichter, C. P. *Phys. Rev.* **1955**, *99*, 479−480.

(96) This is expected for inhomogeneously broadened lines, since their width is due to the hyperfine interactions.

(97) McElroy, J. D.; Feher, G.; Mauzerall, D. C. *Biochim. Biophys. Acta* **1969**, *172*, 180−183.

(98) Norris, J. R.; Uphaus, R. A.; Crespi, H. L.; Katz, J. J. *Proc. Natl. Acad. Sci. U.S.A.* **1971**, *68*, 625−628.

(99) Feher, G.; Hoff, A. J.; Isaacson, R. A.; McElroy, J. D. *Biophys. Soc. Abstr.* **1973**, *13*, 61a.

(100) Norris, J. R.; Druyan, M. E.; Katz, J. J. *J. Am. Chem. Soc.* **1973**, *95*, 1680−1682.

(101) Graige, M. S.; Paddock, M. L.; Bruce, J. M.; Feher, G.; Okamura, M. Y. *J. Am. Chem. Soc.* **1996**, *118*, 9005−9016.

(102) Labahn, A.; Bruce, J. M.; Okamura, M. Y.; Feher, G. *Chem. Phys.* **1995**, *197*, 355−366.

(103) Allen, J. P.; Williams, J. C.; Graige, M. S.; Paddock, M. L.; Labahn, A.; Feher, G.; Okamura, M. Y. *Photosynth. Res.* **1998**, *55*, 227−233.

eqs 33 and 34 to be[104]

$$|V_{if}|^2 \approx (2.3 \pm 0.7) \times 10^{-7}\ (\text{eV})^2 \qquad (36)$$

To compare this result with other estimates, we calculate a maximum electron-transfer rate from eq 26, assuming that the tunneling matrix element is independent of the electron driving force. Thus, from eqs 26 and 36 (and including a factor of $^1/_2$ due to spin selection rules[34]) we obtain

$$(k_{ET})^{max} \approx 10^9\ s^{-1} \qquad (37)$$

Graige et al.[35] estimated a value of $(k_{ET})^{max} \approx 3 \times 10^8\ s^{-1}$ in RCs containing rhodoquinone, a ubiquinone analogue in the Q_B site, which agrees within an order of magnitude with the value of eq 37. The discrepancy between the two values may be partially due to the differences between rhodoquinone and ubiquinone. However, in view of the approximations made in eqs 23, 33, and 34, an order of magnitude agreement of k_{ET} can be considered satisfactory.

Our result (eq 37) is 2 orders of magnitude larger than that expected ($\sim 10^{7.0\pm0.5}\ s^{-1}$) from the most recent compilation of the maximum electron-transfer rate versus distance obtained for many proteins.[36] This discrepancy can be attributed to the intervening protein medium through which the electron transfer occurs, that is the medium between $Q_A^{-\bullet}$ and $Q_B^{-\bullet}$ is a better electron conductor than the *average* medium between the electron donor and acceptor that was used in the compilation. Theories of electron-transfer pathways, that consider the nature of the intervening medium between the two redox partners[105−107] should, in principle, give more reliable estimates of k_{ET}.

Summary and Conclusions

The results of this work can be summarized as follows:

(i) We generated and trapped the biradical state $Q_A^{-\bullet}Q_B^{-\bullet}$ in photosynthetic reaction centers of *Rb. sphaeroides*.

(ii) Frozen samples were studied using EPR at three microwave frequencies, 9.6, 35, and 94 GHz, as a function of temperature between 1.5 and 80 K.

(iii) The spectra of the biradical state $Q_A^{-\bullet}Q_B^{-\bullet}$ differs from that of $Q_A^{-\bullet}$ or $Q_B^{-\bullet}$, due to a magnetic interaction between the quinones.

(iv) The strong temperature dependence of the spectra of the biradical observed provides additional information on the magnetic interactions.

(v) The spectra of the biradical $Q_A^{-\bullet}Q_B^{-\bullet}$ at different frequencies and temperatures were well described using the same parameters of a spin Hamiltonian that includes both dipolar and exchange interactions. The data were fitted using the simulated annealing, Monte Carlo, method.

(vi) The relative geometry of $Q_A^{-\bullet}$ and $Q_B^{-\bullet}$ obtained from the dipolar interaction was in general agreement with crystallographic data.

(vii) A narrowing of the line width of the biradical due to the exchange interaction between the semiquinones was observed.

(viii) The exchange interaction, J_o, was used to estimate a maximum electron-transfer rate of $(k_{ET})^{max} \approx 10^9\ s^{-1}$.

The work described provides information on the *electronic* and *spatial* structure of the biradical. Of particular importance, and relevant to electron transfer, is the value of the exchange interaction J_o, a quantity that is difficult to determine by other methods. Unfortunately, the reported J_o has a relatively large uncertainty, which arises from the insensitivity of the spectra on its value when $|(g_A - g_B)\mu_B B| \ll |J_o|$ (see eq 12). There are several approaches that can be taken to improve the accuracy of J_o: (i) Work at higher magnetic fields where the spectra are more sensitive to J_o. (ii) Produce the biradical in crystals to eliminate the loss of information due to powder averaging. (iii) Measure the change of the hyperfine coupling in the biradical, either by ^{1}H ENDOR,[65] or from the resolved hyperfine structure in the EPR spectra of RCs containing ^{17}O and ^{13}C labeled quinones.[108−110] This approach has been used to calculate the exchange interaction between $Q_A^{-\bullet}$ and Cu^{2+} in RCs where Fe^{2+} was replaced by Cu^{2+}.[111] (iv) Substitute quinones with different *g*-values in the Q_A-site.[112,113] (v) Make judicious mutations (e.g., Ile-L229 → Met)[114] in which the $Q_B^{-\bullet}$ plane is rotated, thereby changing the component of the *g*-value with respect to that of $Q_A^{-\bullet}$.

Concerning the geometry of the biradical, the good agreement between the results obtained from EPR and X-ray crystal structure measurements validates the methodology used in this work. It can, therefore, be applied with confidence to other systems whose structures are not known at molecular resolution, for example, photosystem II of oxygen-evolving organisms.[115] Thus, the work described provides a general procedure to obtain structural information that does not require single crystals.

Acknowledgment. We thank Friedhelm Lendzian for helping with the early measurements and analysis, and Clemens Krucken for technical assistance. This work was supported by Grants from NIH (GM 41637, GM 13191), NSF (MCB 94-16652), Deutsche Forschungsgemeinschaft (Bi 464/7-1), and Fonds der Chemischen Industrie (to R.B. and W.L.).

Note Added in Proof

We have recently performed experiments on $Q_A^{-\bullet}Q_B^{-\bullet}$ at ~330 GHz. (R. A. Isaacson, R. Calvo, G. Feher, A.-L. Maniero,

(104) Since the pathway connecting the two semiquinones should be essentially the same for the first electron transfer, $Q_A^{-\bullet}Q_B \rightarrow Q_AQ_B^{-\bullet}$, as for the electron transfer shown in eq 35, the matrix element should be approximately the same for both processes. Thus, we expect that the maximum electron-transfer rate for the first electron transfer to be approximately the same as that estimated in eq 37.

(105) Skourtis, S. S.; Beratan, D. N. In *Electron Transfer from Isolated Molecules to Biomolecules*; Jortner, J., Bixon, M., Eds.; Wiley: New York, 1999; Vol. 1, pp 377−452.

(106) Regan, J. J.; Onuchic, J. N. In *Electron Transfer from Isolated Molecules to Biomolecules*; Jortner, J., Bixon, M., Eds.; Wiley: New York, 1999; Vol. 2, pp 497−553.

(107) Balabin, I. A.; Onuchic, J. N. In *Biological Physics. Third International Symposium*; Frauenfelder, H., Hummer, G., Garcia, R., Eds.; American Institute of Physics, CP487: Melville, New York, 1999; pp 175−193.

(108) Feher, G.; Isaacson, R. A.; Okamura, M. Y.; Lubitz, W. In *Antennas and Reaction Centers of Photosynthetic Bacteria − Structure, Interactions and Dynamics*; Michel-Beyerle, M.-E., Ed.; Springer Series in Chemical Physics: Berlin, 1985; Vol. 42, pp 174−189.

(109) van den Brink, J. S.; Spoyalov, A P.; Gast, P.; van Liemt, W. B. S.; Raap, J.; Lugtenburg, J.; Hoff, A. J. *FEBS Lett.* **1994**, *353*, 273−276.

(110) Isaacson, R. A.; Abresch, E. C.; Lendzian, F.; Boullais, C.; Paddock, M. L.; Mioskowski, C.; Lubitz, W.; Feher, G. In *The Reaction Center of Photosynthetic Bacteria: Structure and Dynamics*; Michel-Beyerle, M.-E., Ed.; Springer: Berlin, 1996; pp 353−367.

(111) Calvo, R.; Passeggi, M. C. G.; Isaacson, R. A.; Okamura, M. Y.; Feher, G. *Biophys. J.* **1990**, *58*, 149−165.

(112) Okamura, M. Y.; Isaacson, R. A.; Feher, G. *Proc. Natl. Acad. Sci. U.S.A.* **1975**, *72*, 3491−3495.

(113) Woodbury, N. W.; Parson, W. W.; Gunner, M. R.; Prince, R. C.; Dutton, P. L. *Biochim. Biophys. Acta* **1986**, *851*, 6−22.

(114) Paddock, M. L.; Rongey, S. H.; Abresch, E. C.; Feher, G.; Okamura, M. Y. *Photosynth. Res.* **1988**, *17*, 75−96.

(115) Britt, R. D.; Peloquin, J. M.; Campbell, K. A. *Annu. Rev. Biophys. Biomol. Struct.* **2000**, *29*, 463−495.

and L.-C. Brunel, unpublished results). At these high fields, transitions **I** and **III** (see Figure 5) become easily observable. From the positions of these transitions, a more accurate value of J_0 was determined. Its value was within the error of the value quoted in Table 1. A detailed account of this work is in preparation.

JA000399R